



# DNA of Neutrophil Extracellular Traps Binds TMCO6 to Impair CD8<sup>+</sup> T-cell Immunity in Hepatocellular Carcinoma

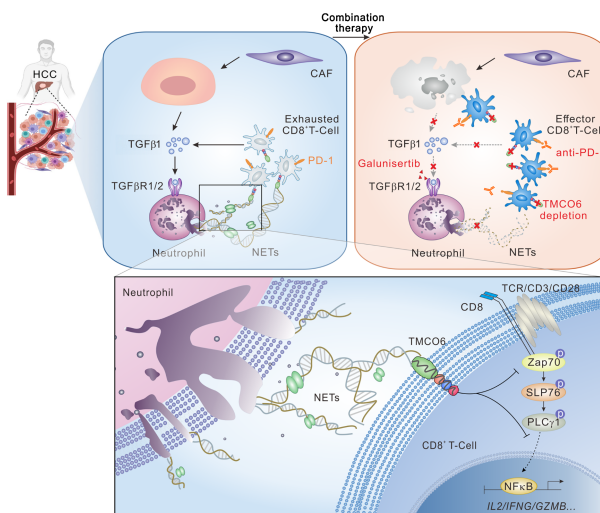
Mengjia Song<sup>1,2</sup>, Chaoqi Zhang<sup>3</sup>, Shaoyan Cheng<sup>4</sup>, Dijun Ouyang<sup>1,5</sup>, Yu Ping<sup>6</sup>, Jieying Yang<sup>1,5</sup>, YaoJun Zhang<sup>1,7</sup>, Yan Tang<sup>1,5</sup>, Hao Chen<sup>1,5</sup>, Qi-jing Wang<sup>1,5</sup>, Yong-qiang Li<sup>1,5</sup>, Jia He<sup>1,5</sup>, Tong Xiang<sup>1,5</sup>, Yizhuo Zhang<sup>1,2</sup>, and Jian-Chuan Xia<sup>1,5</sup>

## ABSTRACT

Neutrophil extracellular traps (NET), formed by the extracellular release of decondensed chromatin and granules, have been shown to promote tumor progression and metastasis. Tumor-associated neutrophils in hepatocellular carcinoma (HCC) are prone to NET formation, highlighting the need for a more comprehensive understanding of the mechanisms of action of NETs in liver cancer. Here, we showed that DNA of NETs (NET-DNA) binds transmembrane and coiled-coil domains 6 (TMCO6) on CD8<sup>+</sup> T cells to impair antitumor immunity and thereby promote HCC progression. TGF $\beta$ 1 induced NET formation, which recruited CD8<sup>+</sup> T cells. Binding to NET-DNA inhibited CD8<sup>+</sup> T cells function while increasing apoptosis and TGF $\beta$ 1 secretion, forming a positive feedback loop to further stimulate NET formation and immunosuppression. Mechanistically, the N-terminus of TMCO6 interacted with NET-DNA and suppressed T-cell receptor signaling and NF $\kappa$ B p65 nuclear translocation. Blocking NET formation by inhibiting PAD4 induced potent antitumor effects in wild-type mice but not TMCO6<sup>-/-</sup> mice. In clinical samples, CD8<sup>+</sup> T cells expressing TMCO6 had an exhausted phenotype. TGF $\beta$ 1 signaling inhibition or TMCO6 deficiency combined with anti-PD-1 abolished NET-driven HCC progression *in vivo*. Collectively, this study unveils the role of NET-DNA in impairing CD8<sup>+</sup> T-cell immunity by binding TMCO6 and identifies targeting

this axis as an immunotherapeutic strategy for blocking HCC progression.

**Significance:** TMCO6 is a receptor for DNA of NETs that mediates CD8<sup>+</sup> T-cell dysfunction in HCC, indicating that the NET-TMCO6 axis is a promising target for overcoming immunosuppression in liver cancer.



## Introduction

The tumor microenvironment (TME) of hepatocellular carcinoma (HCC) contains numerous immune cell types, among which, tumor-associated neutrophils (TAN) are emerging as a key mediator of the immunosuppressive environment that supports HCC development (1). In recent studies from our group (2)

and other colleagues (1, 3, 4), the roles of TANs in impairing the T-cell response have been increasingly recognized, for example, by upregulating programmed cell death 1 ligand, TGF $\beta$ 1 and indoleamine 2,3-dioxygenase 1, recruiting immunosuppressive cells, or inducing oxidative damage, suggesting neutrophils as a potential therapeutic target to improve the efficacy of immune checkpoint blockade. However, it is unclear whether unknown

<sup>1</sup>Collaborative Innovation Center for Cancer Medicine, State Key Laboratory of Oncology in South China, Guangdong Provincial Clinical Research Center for Cancer, Sun Yat-sen University Cancer Center, Guangzhou, P.R. China.

<sup>2</sup>Department of Pediatric Oncology, Sun Yat-sen University Cancer Center, Guangzhou, P.R. China. <sup>3</sup>Department of Thoracic Surgery, National Cancer Center/National Clinical Research Center for Cancer/Cancer Hospital, Chinese Academy of Medical Sciences and Peking Union Medical College, Beijing, P.R. China. <sup>4</sup>Department of Medical Oncology, The Affiliated Cancer Hospital of Zhengzhou University and Henan Cancer Hospital, Zhengzhou, P.R. China. <sup>5</sup>Department of Biotherapy, Sun Yat-sen University Cancer Center, Guangzhou, P.R. China. <sup>6</sup>Department of Biotherapy Center, The First Affiliated Hospital of Zhengzhou University, Zhengzhou, P.R. China.

<sup>7</sup>Department of Hepatobiliary Oncology, Sun Yat-sen University Cancer Center, Guangzhou, P.R. China.

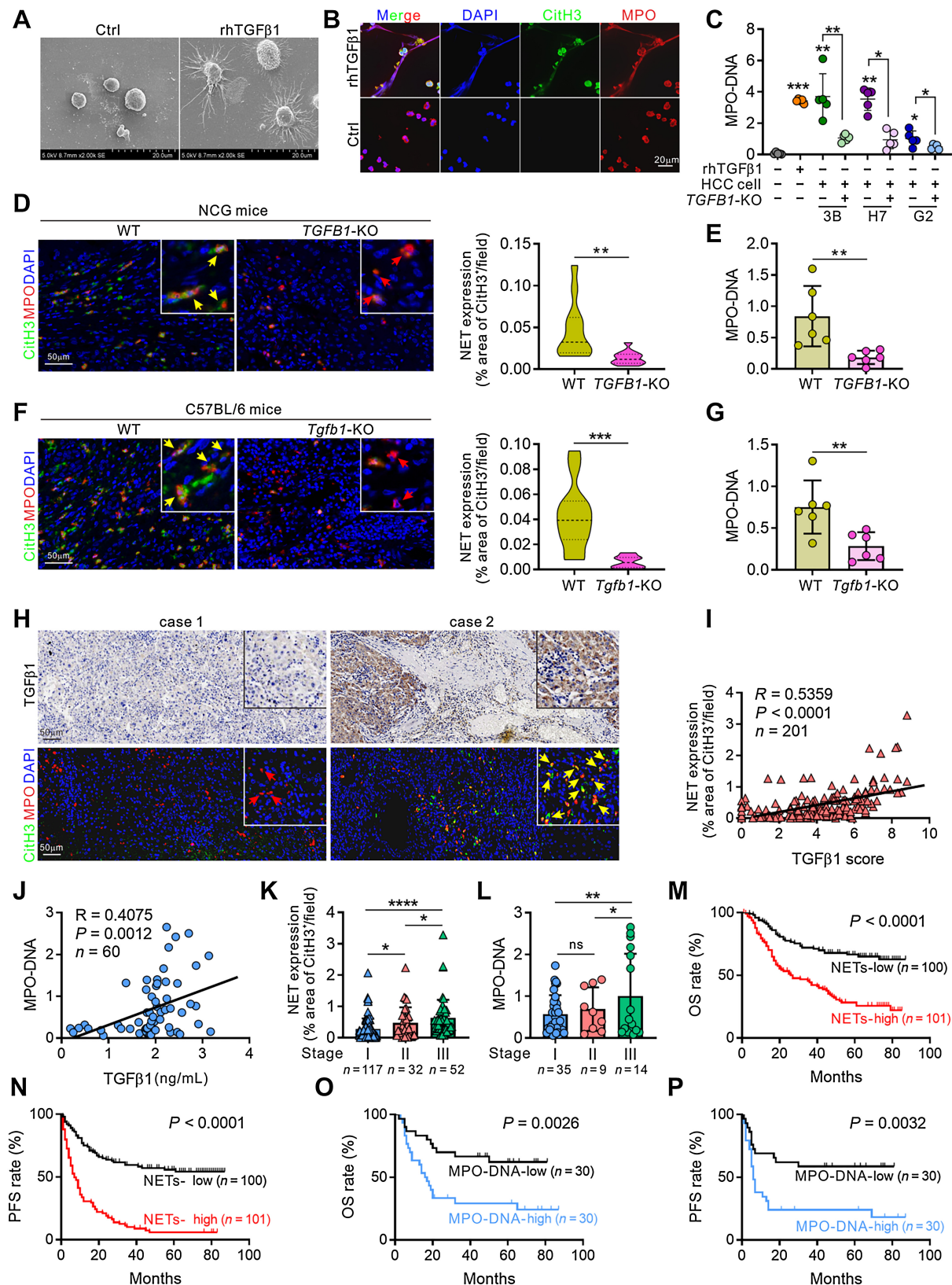
M. Song, C. Zhang, and S. Cheng contributed equally to this article.

**Corresponding Authors:** Jian-Chuan Xia, Sun Yat-sen University Cancer Center, 651 Dongfeng Road East, Guangzhou 510060, P.R. China. E-mail: xiajch@mail.sysu.edu.cn; Yizhuo Zhang, zhangyzh@sysucc.org.cn; and Tong Xiang, xiangtong@sysucc.org.cn

Cancer Res 2024;84:1613–29

doi: 10.1158/0008-5472.CAN-23-2986

©2024 American Association for Cancer Research



mechanisms underlying TAN-mediated immunosuppression exist in HCC progression and how the functional subsets of TANs should be precisely targeted.

“Neutrophil extracellular traps (NET)” have recently emerged as a strong therapeutic target in cancer and other diseases (5). NETs are a large, extracellular, web-like structure composed of nuclear and mitochondrial DNA and cytosolic and granule proteins such as myeloperoxidase (MPO), neutrophil elastase, and actin (6, 7). NET release occurs primarily through a novel cell death process termed “NETosis” upon neutrophil activation (8–11). NETs were first described as a defense mechanism to capture and kill pathogens (6). However, excessive production of NETs has been implicated in inflammation and malignancies (12). Several studies have suggested the role of NETs in cancer progression by directly promoting tumor cell mobilization, trapping circulating tumor cells, awakening dormant cancer cells, increasing vascular permeability, or creating premetastatic niches in various cancers (11, 13, 14). For immune response, NETs reportedly provide physical barriers for the contact of tumor cells with cytotoxic cells (15), selectively express immunosuppressive programmed cell death 1 ligand (16), and regulate the differentiation of regulatory T cells (17). IL17 was revealed to mediate neutrophil recruitment and triggers NETs, and NETs correlate with CD8<sup>+</sup> T-cell exclusion (18). Our previous study showed that “N2”-polarized TANs are prone to NET formation in HCC (2). Despite these aspects of NETs, limited data are available regarding their exact role in modulating CD8<sup>+</sup> T-cell immunity.

Here, we investigated the role of DNA of NETs (NET-DNA) in impairing CD8<sup>+</sup> T-cell immunity, identified the specific receptor of NET-DNA and the downstream signaling pathways, and explored the application of potential related immunotherapeutic target and predictive biomarker for HCC.

## Materials and Methods

### Study approval

This study was approved by the Institutional Review Board of Sun Yat-Sen University Cancer Center (Guangzhou, P.R. China). The approval number for human studies is GZR2019-287, and the approval number for animal studies is L102012021050N. All experiments involving humans were carried out in accordance with the Code of Ethics of the World Medical Association (Declaration of Helsinki), and written informed consents were obtained from all patients before inclusion. All animal procedures complied with the Guide for the Care and Use of Laboratory Animals criteria of the National Academy of Sciences.

### Patient sample collection

All human samples were obtained from Sun Yat-Sen University Cancer Center (Guangzhou, P.R. China). For IHC staining, immunofluorescence (IF) staining, and ELISA, 201 paraffin-embedded tissues and 60 frozen serum samples were collected from patients with primary HCC between 2005 and 2008, and 51 paraffin-embedded tissues and 30 frozen serum samples were collected from patients with primary hepatoblastoma (HB) between 2013 and 2018. For isolating patient-derived peripheral blood mononuclear cells (PBMC), tumor-infiltrating lymphocytes (TIL), and tumor interstitial fluid (TIF), fresh peripheral blood and tumor tissues were obtained from 20 patients with primary HCC. All samples in the study were confirmed by pathologic analysis. None of the patients with HCC received any therapeutic intervention before surgery. All patients with HB with metastasis received chemotherapy before surgery.

### Cell lines and culture

Human HCC cell lines Hep3B (RRID: CVCL\_0326) and Huh7 (RRID: CVCL\_0336), murine HCC cell line Hepa1-6 (RRID: CVCL\_0327), human T lymphocyte cell line Jurkat, Clone E6-1 (RRID: CVCL\_0367), and human HB cell lines HepG2 (RRID: CVCL\_0027) and Huh6 (RRID: CVCL\_4381) were purchased from the ATCC. All cell lines were used within 15 passages. All cell line authentication had been carried out by short tandem repeat method through using Short Tandem Repeat Multi-Amplification Kit (Microreader 21 ID System), which was used for PCR amplification and PCR products were detected by ABI 3130xl DNA Analyzer (Applied Biosystems). All cell lines had been confirmed without *Mycoplasma* contamination by using Mycoplasma Stain Assay Kit (Beyotime Institute of Biotechnology). Tumor cells were cultured in DMEM (Gibco, Invitrogen) supplemented with 10% FBS (Gibco), 100 U/mL penicillin, and 100 U/mL streptomycin in 5% CO<sub>2</sub> at 37°C. Jurkat cells were cultured in RPMI1640 medium (Gibco) supplemented with 10% FBS (Gibco), 100 U/mL penicillin, and 100 U/mL streptomycin in 5% CO<sub>2</sub> at 37°C.

### TIF isolation

Fresh tissues were placed on a triple-layered 10-μm nylon mesh and spun at <50 × g for 5 minutes to remove the surface liquid. Then, samples were centrifuged at 400 × g for 10 minutes to isolate the TIF (19).

### Purification and quantification of NETs

Human neutrophils were isolated from the peripheral blood of healthy donor, and murine neutrophils were isolated from the

### Figure 1.

TGFβ1-induced NETs are closely associated with poor prognosis in patients with HCC. **A**, Human neutrophils were isolated from healthy donors. Representative electron micrographs of control or rhTGFβ1 (10 ng/mL)-treated neutrophils (NETs) for 3 hours. Scale bar, 20 μm. **B**, IF staining for the colocalization of CitH3 (green), MPO (red), and DAPI (blue) in control or rhTGFβ1-treated neutrophils for 3 hours. NETs were costained with CitH3, MPO, and DAPI. **C**, Human neutrophils were treated with rhTGFβ1 or cocultured with WT or *TGFβ1*-KO liver cancer cells for 3 hours. Indicated supernatants were collected for the detection of MPO-DNA. **D** and **F**, Representative photomicrographs of IF staining for the colocalization of CitH3 (green), MPO (red), and DAPI (blue) in indicated subcutaneous tumors harvested from NCG mice (**D**) or C57BL/6 mice (**F**). Yellow arrows indicate NETs, costained with CitH3, MPO, and DAPI, and red arrows indicate normal neutrophils. Scale bars, 50 μm. CitH3-positive areas representing NET expression are shown as a statistical graph; *n* = 6 for each group. **E** and **G**, Serum levels of MPO-DNA in NCG mice (**E**) or C57BL/6 mice (**G**). **H**, Representative photomicrographs for consecutive sections of HCC tissues show the expression TGFβ1 by IHC staining and the expression pattern of CitH3 (green), MPO (red), and DAPI (blue) by IF staining. Scale bar, 50 μm. **I**, Correlation between TGFβ1 score and the positive areas of CitH3 representing NET expression was analyzed in 201 HCC tissues. **J**, Correlation between serum levels of TGFβ1 and MPO-DNA was analyzed in 60 patients with HCC. **K**, The positive areas of CitH3 representing NET expression in HCC tissues from different stages. **L**, Serum levels of MPO-DNA in patients with HCC from different stages. **M–P**, Kaplan–Meier curves for OS and PFS in patients with HCC with low and high NET expression based on IF staining (**M** and **N**) or serum-level MPO-DNA (**O** and **P**). The median value was considered as the cut-off value to define low or high expression. 3B, Hep 3B; H7, Huh7; G2, HepG2. Data are representative of three independent experiments. \*, *P* < 0.05; \*\*, *P* < 0.01; \*\*\*, *P* < 0.001; \*\*\*\*, *P* < 0.0001, by one-way ANOVA for the multiple comparisons (**C**, **K**, and **L**), Student *t* test (**D**–**G**), Pearson correlation analysis (**I** and **J**) or log-rank test (**M**–**P**). ns, nonsignificant.

peripheral blood of C57BL/6 mice. Human neutrophils were treated with recombinant human TGF $\beta$ 1 (10 ng/mL, Peprotech), phorbol-12-myristate-13-acetate (PMA; 500 nmol/L, Sigma-Aldrich), or lipopolysaccharide (LPS; 1  $\mu$ g / mL, Sigma-Aldrich) or cocultured with HCC cell lines in Transwell system for 3 hours. In some experiments, human neutrophils were cultured with supernatants collected from human CD8 $^{+}$  T cells treated under the indicated conditions for 3 hours. After removing the supernatant, NETs adhered at the bottom were washed down by pipetting 2 mL of cold PBS and centrifuged at 1,000  $\times g$  for 10 minutes at 4°C. Cell-free supernatants containing NETs (DNA-protein complex) were harvested and used for further experiments. The DNA concentration of NETs was measured by spectrophotometry using a Nano Drop 2000 (Thermo Fisher Scientific). In detail, Nano drop can detect the absorbance signal of the sample in the spectral range including UV and visible light, and the DNA has a maximum absorbance at 260 nm. On the basis of the absorbance, the concentration of DNA in the sample can be calculated. Serum NETs were quantified by analyzing the MPO-DNA complex level using a previously described method (16). The median value was considered as the cut-off value to define low or high expression.

#### Biotinylated NET-DNA pulldown assay

DNA pulldown assay was performed according to a similar method, which was previously described elsewhere (20). NET-DNA were purified and labeled with biotin, and membrane proteins were isolated from human CD8 $^{+}$  T cells or Jurkat cells transfected with flag-transmembrane and coiled-coil domains 6 (TMCO6) plasmids. Next, 2 mg membrane proteins were incubated with or without 500 ng biotinylated NET-DNA in 400  $\mu$ L immunoprecipitation (IP) lysis buffer (Thermo Fisher Scientific) at room temperature for 1 hour followed by incubation with 50  $\mu$ L Streptavidin Magnetic Beads (MedChemExpress) at room temperature for 30 minutes. The beads were then washed five times with IP lysis Buffer and collected by magnetic separation. The samples were eluted with Lane Marker Reducing Sample (Invitrogen) and further used for gradient gel electrophoresis and subsequent silver staining. The differential bands were analyzed by LC/MS-MS.

In some experiments of NET-DNA pulldown assay involving human CD8 $^{+}$  T cells, the eluted samples were analyzed by immunoblotting with anti-TMCO6 antibody (1:1,000, Thermo Fisher Scientific); in some experiments of NET-DNA pulldown assay involving Jurkat cells transfected with flag-TMCO6 plasmids, the eluted samples were analyzed by immunoblotting with anti-flag antibody (1:1,000, Sigma-Aldrich).

#### IHC staining and evaluation

The IHC staining protocol was described elsewhere (21). The following anti-human primary antibodies were used: TGF $\beta$ 1 (Abcam, 1:500), anti-granzyme B (Abcam, 1:3,000), and anti-TMCO6 (Thermo Fisher Scientific, 1: 500). The intensity of IHC staining was assessed using the following criteria: 0, none; 1, light yellow; 2, dark yellow; and 3, brown. The extent of IHC staining was scored as 0, >0 and  $\leq$ 3% stained; 1, >3% and  $\leq$ 5% stained; 2, >5% and  $\leq$ 10% stained; and 3, >10% stained. Five random fields per sample were evaluated using a light microscope (Olympus). The final scores were calculated by multiplying the intensity scores by the extent scores. The median value was considered as the cut-off value to define low or high expression of indicated markers.

#### Electron microscopy scanning

For the visualization of NETs, neutrophils were stimulated with or without recombinant human (rh)TGF $\beta$ 1 (10 ng/mL, Peprotech) on poly-L-lysine-coated glass coverslips at 37°C for 3 hours. Cells were fixated with electron microscopy fixation solution consisting of 2.5% glutaraldehyde with 0.1 mol/L phosphoric acid buffer as solvent for 1 hour at room temperature and then for an additional 8 hours at 4°C. The samples were successively dehydrated with 30%, 50%, 70%, 90%, 100%, and 100% ethanol gradient for 15 minutes, and then dried using a supercritical dryer (Autosamdry-815, Toussimis). The sample was then sputtered with gold (Ion Sputter MC1000, Hitachi) and finally analyzed using a scanning electron microscopy (SU8020, Hitachi).

#### Western blot analysis

The Western blot protocol was described elsewhere (2). Nucleus proteins were extracted using a Nuclear and Cytoplasmic Protein Extraction Kit (Beyotime Biotechnology) according to the manufacturer's instructions. TATA-box-binding protein (TBP) was used as a control for nucleus proteins. Primary anti-human antibodies used were as follows: TGF $\beta$ 1 (1:1,000, Abcam), TMCO6 (1:1,000, Thermo Fisher Scientific), citrullinated histone H3 (CitH3; 1:1,000, Abcam), Src (1:1,000, Cell Signaling Technology), phospho-Src (1:1,000, Cell Signaling Technology), Zap-70 (1:1,000, Cell Signaling Technology), phospho-Zap-70 (1:1,000, Cell Signaling Technology), SLP-76 (1:1,000, Cell Signaling Technology), phospho-SLP-76 (1:1,000, Cell Signaling Technology), PLC $\gamma$ 1 (1:1,000, Cell Signaling Technology), phospho-PLC $\gamma$ 1 (1:1,000, Cell Signaling Technology), NF $\kappa$ B p65 (1:1,000, Cell Signaling Technology), TBP (1:1,000, Proteintech Group), and  $\beta$ -actin (1:5,000, Cell Signaling Technology). Primary anti-mouse antibodies used were as follows: TGF $\beta$ 1 (1:1,000, Abcam) and  $\beta$ -actin (1:5,000, Cell Signaling Technology).

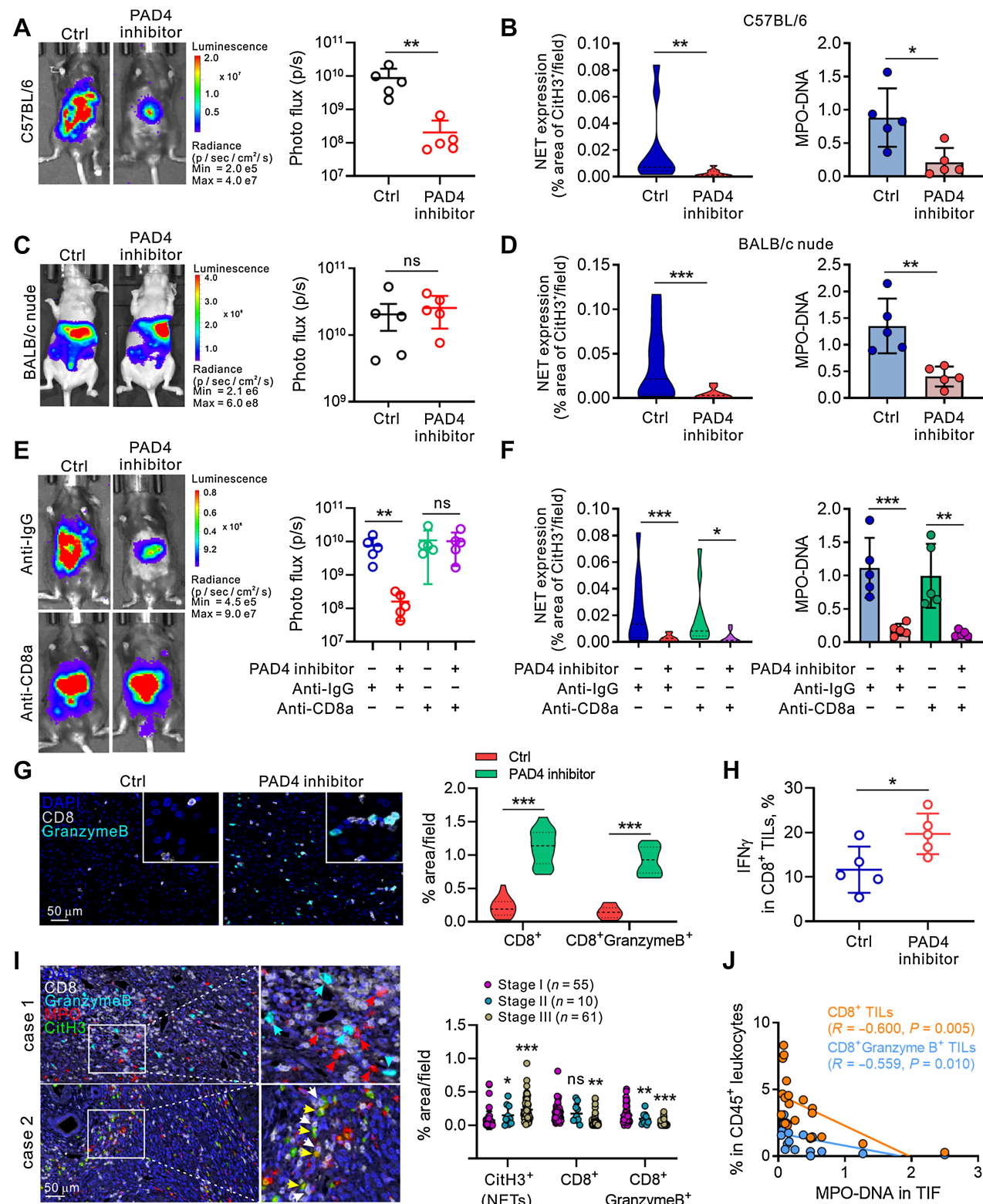
#### Flow cytometry analysis

Flow cytometry analysis was performed to assess the surface expression of CD25, CD69, PD-1, TIM3, and LAG3, intracellular expression of IFN $\gamma$ , granzyme B, and TGF $\beta$ 1, nuclear expression of Ki67 by indicated CD8 $^{+}$  T cells. For the staining of CD8 $^{+}$  T cells from the PBMC of human healthy donors, isolated CD8 $^{+}$  T cells were stained with anti-7-aminoactinomycin D (7AAD) for surface staining or Fixable Viability Stain 575V (FVS575V; BD Biosciences) for intracellular and nuclear staining, anti-human CD8, anti-human IFN $\gamma$ , anti-human granzyme B, anti-human CD25, anti-human CD69, anti-human Ki67, anti-human TGF $\beta$ 1, and anti-human PD-1. For the staining of CD8 $^{+}$  TILs from patients with HCC, isolated TILs were stained with Fixable Viability Stain, anti-human CD45, anti-human CD8, and anti-human granzyme B. For the staining of TILs from mouse tumors, tumor tissues were minced, and the tissue homogenate was then filtered through a 40- $\mu$ m filter to isolate single cells. CD8 $^{+}$  T cells were identified with CD45 and CD8. CD4 $^{+}$  T cells were identified with CD45 and CD4. Natural killer (NK) cells were identified with CD45, CD3 and NKp46. In experiments involving adoptive transfer, transferred CD8 $^{+}$  T cells were identified with CD45.2 and CD8. To examine the expression of IFN $\gamma$ , CD25, CD69, Ki67, PD-1, TIM3, and LAG3 by mouse CD8 $^{+}$  T cells, isolated cells were stained with anti-7AAD for surface staining or Fixable Viability Stain for intracellular and nuclear staining, anti-mouse CD45, anti-mouse CD8, anti-mouse IFN $\gamma$ , anti-mouse CD25, anti-mouse CD69, anti-mouse Ki67, anti-mouse PD-1, anti-mouse TIM3, and anti-mouse LAG3. To examine the expression of IL2, IFN $\gamma$ , IL4, and IL10 by mouse CD4 $^{+}$  T cells, isolated cells were stained with Fixable Viability Stain, anti-mouse CD45, anti-mouse CD4, anti-mouse IL2,

**Table 1.** Univariate and multivariate analysis of OS and PFS in patients with HCC.

Variable	Tumor tissue (n = 201)						Serum (n = 60)					
	Overall survival			Progression-free survival			Overall survival			Progression-free survival		
	Univariate Cox	Multivariate Cox	HR	Univariate Cox	Multivariate Cox	HR	Univariate Cox	Multivariate Cox	HR	Univariate Cox	Multivariate Cox	HR
<b>Age (year)</b>												
≥50 or <50	0.806	0.952 (0.644-1.407)		0.486 (0.802-1.592)	1.130 (0.581-1.478)		0.927 (0.469-1.995)	0.967 (0.469-1.995)		0.849 (0.470-1.863)	0.935 (0.571-2.961)	
<b>Gender</b>												
Male or female	0.822	1.065 (0.616-1.841)		0.750 (0.581-1.478)	0.927 (0.463-2.460)		0.879 (0.463-2.460)	1.067 (0.329-5.760)		0.533 (0.474-8.213)	1.300 (0.571-2.961)	
<b>HBsAg</b>												
Positive or negative	0.832	1.063 (0.605-1.967)		0.565 (0.709-1.875)	1.153 (0.695-1.452)		0.661 (0.069-0.749)	1.377 (0.043-17.12)		0.351 (0.222-1.287)	1.973 (0.571-2.961)	
<b>Liver cirrhosis</b>												
Yes or no	0.460	1.174 (0.768-1.794)		0.980 (0.695-1.452)	1.005 (0.695-1.452)		0.015 (0.069-0.749)	0.228 (0.043-17.12)		0.162 (0.474-8.213)	0.535 (0.571-2.961)	
<b>Tumor size</b>												
≥5cm or <5cm	0.002	1.918 (1.268-2.901)	0.329 (0.794-1.986)	0.001 (1.318-2.773)	1.895 (0.105-2.248)	0.042 (0.523-2.425)	1.510 (0.204-0.478)	0.762 (0.624-2.735)	1.126 (0.307-2.735)	0.586 (0.345-5.001)	1.224 (0.592-2.531)	
<b>TNM stage</b>												
II-III or I	<0.001	2.547 (1.726-3.758)	0.802 (0.432-1.915)	0.909 (1.700-3.399)	<0.001 (0.654-2.260)	0.537 (0.1025-4.059)	1.215 (0.2040-0.478)	0.042 (0.624-2.735)	2.040 (0.624-2.735)	0.478 (0.307-2.735)	0.004 (0.294-1.287)	0.504 (0.605-2.776)
<b>Tumor encapsulation</b>												
Yes or no	0.180	0.767 (0.520-1.131)		0.371 (0.607-1.207)	0.855 (0.607-1.207)		0.006 (0.081-0.662)	0.231 (0.131-3.840)	0.691 (0.095-1.028)	0.710 (0.058-0.448)	0.058 (0.592-2.531)	
<b>Tumor number</b>												
Multiple or single	0.003	1.794 (1.129-2.640)	0.047 (0.006-2.275)	1.513 (1.272-2.531)	0.001 (0.875-1.470)	1.795 (1.028-2.132)	0.035 (0.1600-28.120)	1.480 (0.272-29.85)	0.009 (0.272-29.85)	6.707 (0.272-29.85)	0.382 (0.272-29.85)	0.036 (0.1075-8.712)
<b>AFP (ng/mL)</b>												
≥400 or <400	0.807	0.952 (0.641-1.413)		0.231 (0.875-1.470)	1.234 (0.875-1.470)		0.505 (0.631-2.5510)	1.268 (0.483-5.198)		0.407 (0.634-2.549)	1.321 (1.118-10.09)	
<b>Histologic differentiation</b>												
Poor or well	0.007	1.809 (1.172-2.793)	0.634 (0.654-2.005)	1.146 (1.234-2.915)	0.057 (1.381-3.316)	1.473 (0.693-1.893)	0.447 (0.838-3.887)	1.585 (0.483-5.198)		0.353 (0.579-4.619)	1.635 (0.592-4.619)	
<b>Vasculinvasive</b>												
Yes or no	<0.001	2.517 (1.550-4.069)	0.343 (0.747-2.311)	1.314 (1.381-3.316)	0.001 (2.364-4.850)	2.140 (2.364-4.850)	0.595 (0.727-2.611)	1.146 (0.401-1.860)	1.805 (0.838-3.887)	<0.001 (0.450-1.930)	4.210 (1.700-9.198)	3.954 (0.875-3.949)
<b>Distant metastasis</b>												
Yes or no	<0.001	3.729 (2.508-5.545)	0.021 (1.145-5.325)	2.469 (1.863-6.060)	<0.001 (2.041-4.854)	3.386 (2.863-6.060)	0.326 (2.041-4.854)	1.378 (1.388-5.994)	0.708 (1.225-5.701)	0.864 (1.225-5.701)	0.849 (1.282-5.034)	1.859 (0.875-3.949)
<b>NETs</b>												
High or low	<0.001	2.912 (1.929-4.395)	0.008 (1.184-3.032)	1.895 (2.863-6.060)	<0.001 (2.041-4.854)	4.165 (3.147-4.854)	0.005 (2.041-4.854)	2.885 (1.388-5.994)	0.013 (1.225-5.701)	2.643 (1.225-5.701)	0.008 (1.282-5.034)	2.541 (1.282-5.034)

Abbreviations: ELISA, enzyme-linked immunosorbent assay; HCC, hepatocellular carcinoma; IHC, immunohistochemistry; OS, overall survival; PFS, progression-free survival.

**Figure 2.**

NETs facilitate HCC progression by impairing CD8<sup>+</sup> T-cell immunity. **A** and **C**, Tumor growth of C57BL/6 mice (**A**) or BALB/c nude mice (**C**) treated with or without PAD4 inhibitor, Cl-amidine (10 mg/kg/day, intraperitoneally), was measured using an *in vivo* imaging system at 4 weeks after tumor implantation. *n* = 5 for each group. **B** and **D**, CitH3-positive areas representing NET expression in tumors (left) and serum levels of MPO-DNA (right) are shown as a statistical graph in indicated mice. (Continued on the following page.)

anti-mouse IFN $\gamma$ , anti-mouse IL4, and anti-mouse IL10. To examine the expression of IFN $\gamma$  and granzyme B by mouse NK cells, isolated cells were stained with Fixable Viability Stain, anti-mouse CD45, anti-mouse CD3, anti-mouse NKP46, anti-mouse IFN $\gamma$ , and anti-mouse granzyme B. For cytokine detection, cells were stimulated with PMA and ionomycin (Sigma-Aldrich) in the presence of a protein transport inhibitor brefeldin A (BioLegend) for 6 hours, and then stained with fluorochrome-conjugated primary antibodies. For Jurkat cells transfected with full-length human TMCO6 tagged with Flag at the N-terminus (Flag-TMCO6) or C-terminus (TMCO6-Flag), flow cytometry analysis was performed for Flag signal with PE anti-DYKDDDDK (flag) Tag antibody by surface and intracellular staining. All the antibodies were purchased from BD Biosciences or BioLegend. Intracellular staining and surface staining were performed as described previously (21), and Fixation/Permeabilization Solution Kit (BD Biosciences) according to the manufacturers' instructions. Nuclear staining was performed by using a Transcription Factor Staining Buffer Set (Thermo Fisher Scientific). Fixable Viability Stain 575V used to gate live cells in intracellular and nuclear staining can be excited by violet laser-equipped Flow Cytometers. According to the manufacturer's instruction, cells were stained with Fixable Viability Stain in serum-free buffer. Then, cells were washed, fixed, and permeabilized for intracellular or nuclear staining.

The representative dotplots used for gating strategies of CD8<sup>+</sup> T cells from the PBMC of human healthy donors were shown in Supplementary Fig. S1A–S1D. The representative dotplots used for gating strategies of CD8<sup>+</sup> granzyme B<sup>+</sup> TILs from human HCC tissues were shown in Supplementary Fig. S1E. The representative dotplots used for gating strategies of CD8<sup>+</sup> T cells from the mouse models were shown in Supplementary Figs. S2A–S2C and S3A. The representative dotplots used for gating strategies of NK cells and CD4<sup>+</sup> T cells from the mouse models were shown in Supplementary Fig. S3A. The representative dotplots used for gating strategies of the CD8<sup>+</sup> IFN $\gamma$ <sup>+</sup> and CD8<sup>+</sup> granzyme B<sup>+</sup> TILs from mouse tumor tissues were shown in Supplementary Fig. S3B.

#### Statistical analysis

Statistical analyses were performed using SPSS (RRID: SCR\_002865) version 20.0 or Prism 8 (Graph Pad Software Inc.). Data are expressed as the mean  $\pm$  SD according to the distribution level. Differences between groups with normally distributed continuous variables were analyzed using Student *t* test. For multiple comparisons, a one-way ANOVA was used as noted in the figure legends. The association between the expression levels of two markers was analyzed using Pearson correlation coefficient. The Kaplan-Meier method and log-rank test were used to plot survival curves and analyze differences in survival time between patient subgroups. A  $\chi^2$  test was

used to assess the correlation between NET-related biomarkers and the clinicopathologic characteristics of patients with HCC. Cox proportional hazards regression model was used to evaluate the prognostic values of the risk factors. To determine the diagnostic values of NET-related biomarkers in patients with HCC and HB, ROC analyses were performed, the AUC were reported, and the sensitivity and specificity were calculated to facilitate the measurement of the diagnostic values. The Wilcoxon-Mann-Whitney test was used to compare non-normal distribution continuous variables between two groups in single-cell RNA sequencing (scRNA-seq) analysis. In all analyses, a two-tailed  $P < 0.05$  was considered statistically significant, \*,  $P < 0.05$ ; \*\*,  $P < 0.01$ ; \*\*\*,  $P < 0.001$ ; \*\*\*\*,  $P < 0.0001$ .

## Results

### TGF $\beta$ 1 secreted by tumor cells induces NET formation

Cancer-associated fibroblast-mediated TGF $\beta$ 1 production by HCC cells was preliminarily found to induce NETosis of neutrophils in our previous study (2). We further observed the abundant presence of extracellular net-like structures in recombinant human TGF $\beta$ 1 (rhTGF $\beta$ 1)-treated neutrophils (Fig. 1A). Multilobed nuclei and MPO were contained in untreated neutrophil borders; however, upon stimulation with rhTGF $\beta$ 1, we observed nuclei with some extruding extracellular DNA that colocalized with MPO and CitH3, a specific biomarker of NETosis (Fig. 1B; ref. 22). Meanwhile, we assessed NET levels in the supernatants by the MPO-DNA complex (23) and obtained similar results (Fig. 1C).

We next examined the effects of tumor-derived TGF $\beta$ 1 on NET formation. Supernatants from neutrophils cocultured with wild-type (WT) Hep3B and Huh7 that express high-level TGF $\beta$ 1 showed much higher levels of NETs than those from coculture with HepG2 that expresses low-level TGF $\beta$ 1, whereas *TGF $\beta$ 1* knockout (KO; Fig. 1C; Supplementary Fig. S4A–S4C) or 1D11, a TGF $\beta$ 1, 2 and 3 neutralizing antibody, severely impaired NETs induced by all cell lines

(Continued.) **E** and **F**, Anti-IgG or anti-CD8a antibodies-treated C57BL/6 mice were administered with or without PAD4 inhibitor, Cl-amidine (10 mg/kg/day, intraperitoneally). **E**, Tumor growth was measured using an *in vivo* imaging system at 4 weeks after tumor implantation.  $n = 5$  for each group. **F**, CitH3-positive areas representing NET expression in tumors (left) and serum levels of MPO-DNA (right) are shown as a statistical graph. **G**, Representative photomicrographs of IF staining for the colocalization of CD8 (white), granzyme B (cyan), and DAPI (blue) in tumors from C57BL/6 mice treated with or without PAD4 inhibitor. Scale bars, 50  $\mu$ m. CD8-positive areas and CD8 and granzyme B double-positive areas are shown as statistical graphs. **H**, Flow cytometry analysis for the expression of IFN $\gamma$  by CD8<sup>+</sup> TILs infiltrated in tumors from C57BL/6 mice treated with or without PAD4 inhibitor. **I**, Left, IF staining for the coexpression pattern of CD8 (white), granzyme B (cyan), CitH3 (green), MPO (red), and DAPI (blue) in tumor tissues from patients with HCC. Scale bars, 50  $\mu$ m. Right, CitH3-positive areas representing NET expression, CD8-positive areas, and CD8 and granzyme B double-positive areas in tumor tissues from different stages are shown as statistical graphs. **J**, TILs and TIF were isolated from fresh tumor tissues of 20 patients with HCC. The frequencies of CD8<sup>+</sup> TILs and CD8<sup>+</sup> granzyme B<sup>+</sup> TILs in CD45<sup>+</sup> leukocytes were examined by flow cytometry. The levels of MPO-DNA in TIF was detected. Correlation analyses were performed using Pearson correlation method. Data are representative of three independent experiments. \*,  $P < 0.05$ ; \*\*,  $P < 0.01$ ; \*\*\*,  $P < 0.001$ , by Student *t* test (**A–D** and **H**), one-way ANOVA for the multiple comparisons (**E–G** and **I**) or Pearson correlation analysis (**J**). ns, nonsignificant.

(Supplementary Fig. S4D). By employing xenograft mouse models (**Fig. 1D** and **E**; Supplementary Fig. S4E and S4F), we found more abundant NETs in WT group than those of *TGFB1*-KO group. Similar results were observed in a syngeneic subcutaneous mouse model in C57BL/6 mice (**Fig. 1F** and **G**) using Hepa1-6, a murine HCC cell line that express TGF $\beta$ 1 (Supplementary Fig. S4A and S4C). However, administration of 1D11 remarkably decreased the NET levels in mouse (Supplementary Fig. S4G and S4H), further confirming that TGF $\beta$ 1 directly induces NETosis.

In clinical samples, TGF $\beta$ 1 was dominantly expressed in the tumoral region (**Fig. 1H**). TGF $\beta$ 1 had a positive correlation with NETs in both primary tumor (**Fig. 1H** and **I**) and serum (**Fig. 1J**) levels. Taken together, these results indicate that tumor cell-derived TGF $\beta$ 1 can induce NET formation in HCC.

#### **NETs are positively correlated with tumor progression and poor prognosis in patients with HCC**

NETs in tumor tissue (**Fig. 1K**) and MPO–DNA complex in serum (**Fig. 1L**) were significantly upregulated as tumor stage increased. Correlation analysis (Supplementary Table S1) revealed a close relationship between a high expression level of NETs in tumor tissues and tumor size, tumor–node–metastasis stage, histologic differentiation, vascular invasion, and distant metastasis, and a high serum level of the MPO–DNA complex was closely associated with tumor size, tumor number, and distant metastasis. Patients with high levels of NETs had poor overall survival (OS) and progression-free survival (PFS; **Fig. 1M–P**). NETs in tumor tissues were an independent prognostic indicator for OS and PFS, and the MPO–DNA complex in serum was an independent prognostic indicator for OS (**Table 1**). NETs had good sensitivity and specificity for predicting OS and PFS (Supplementary Fig. S5A and S5B). Overall, these results suggest that NETs are a clinically noteworthy factor that may play a crucial role in HCC progression.

#### **NETs facilitate HCC progression by impairing CD8 $^{+}$ T-cell immunity**

Peptidylarginine deiminase 4 (PAD4) is a key enzyme required for NET formation (24). NET formation induced by TGF $\beta$ 1 was efficiently abrogated upon inhibiting PAD4 activity with a pharmacologic inhibitor, Cl-amidine (Supplementary Fig. S6A; ref. 25). PAD4 inhibitor dramatically reduced HCC growth and NET formation in immunocompetent C57BL/6 mice (**Fig. 2A** and **B**; Supplementary Fig. S6B), suggesting that NETs serve as a key determinant in HCC development. Strikingly, PAD4 inhibition disrupted NET formation but had no effect on tumor growth in immunodeficient NCG and BALB/c nude mice (**Fig. 2C** and **D**; Supplementary Fig. S6C–S6F), implying that the protumorigenic role of NETs may be dependent on the impairment of T-cell immunity. Indeed, after depleting CD8 $^{+}$  T cells from C57BL/6 mice, no significant difference was observed in tumor development between the control and PAD4 inhibitor treatment groups (**Fig. 2E**), despite the fact that PAD4 inhibition eliminated NET formation (**Fig. 2F**; Supplementary Fig. S6G). This supports the notion that NETs promote HCC progression by disrupting CD8 $^{+}$  T-cell immunity. Consistently, PAD4 inhibitor increased the infiltration of CD8 $^{+}$  T cells and their expression of granzyme B and IFN $\gamma$  in C57BL/6 mouse tumors (**Fig. 2G** and **H**; Supplementary Fig. S6H).

Next, we adoptively transferred TGF $\beta$ 1-induced NETs into tumor-bearing C57BL/6 mice (Supplementary Fig. S6I). Adoptive transfer of NETs accelerated HCC progression (Supplementary Fig. S6J), concomitant with decreased infiltration of CD8 $^{+}$ , CD8 $^{+}$  IFN $\gamma$  $^{+}$ , and

CD8 $^{+}$  granzyme B $^{+}$  TILs (Supplementary Fig. S6K), further confirming that NETs impair CD8 $^{+}$  T-cell immunity *in vivo*. In clinical samples (**Fig. 2I**), abundant NET structure and CD8 $^{+}$  T cells were physically adjacent; moreover, with the increase of tumor stage, the expression level of NETs increased, while the infiltration of CD8 $^{+}$  T cells and CD8 $^{+}$  granzyme B $^{+}$  T cells decreased. In addition, we isolated TILs and TIF from the fresh HCC tissues of patients. The level of the MPO–DNA complex in TIF was negatively correlated with the frequencies of CD8 $^{+}$  TILs and CD8 $^{+}$  granzyme B $^{+}$  TILs (**Fig. 2J**). Together, these results indicate the potential role of NETs in negatively modulating CD8 $^{+}$  T-cell immunity in the TME of HCC.

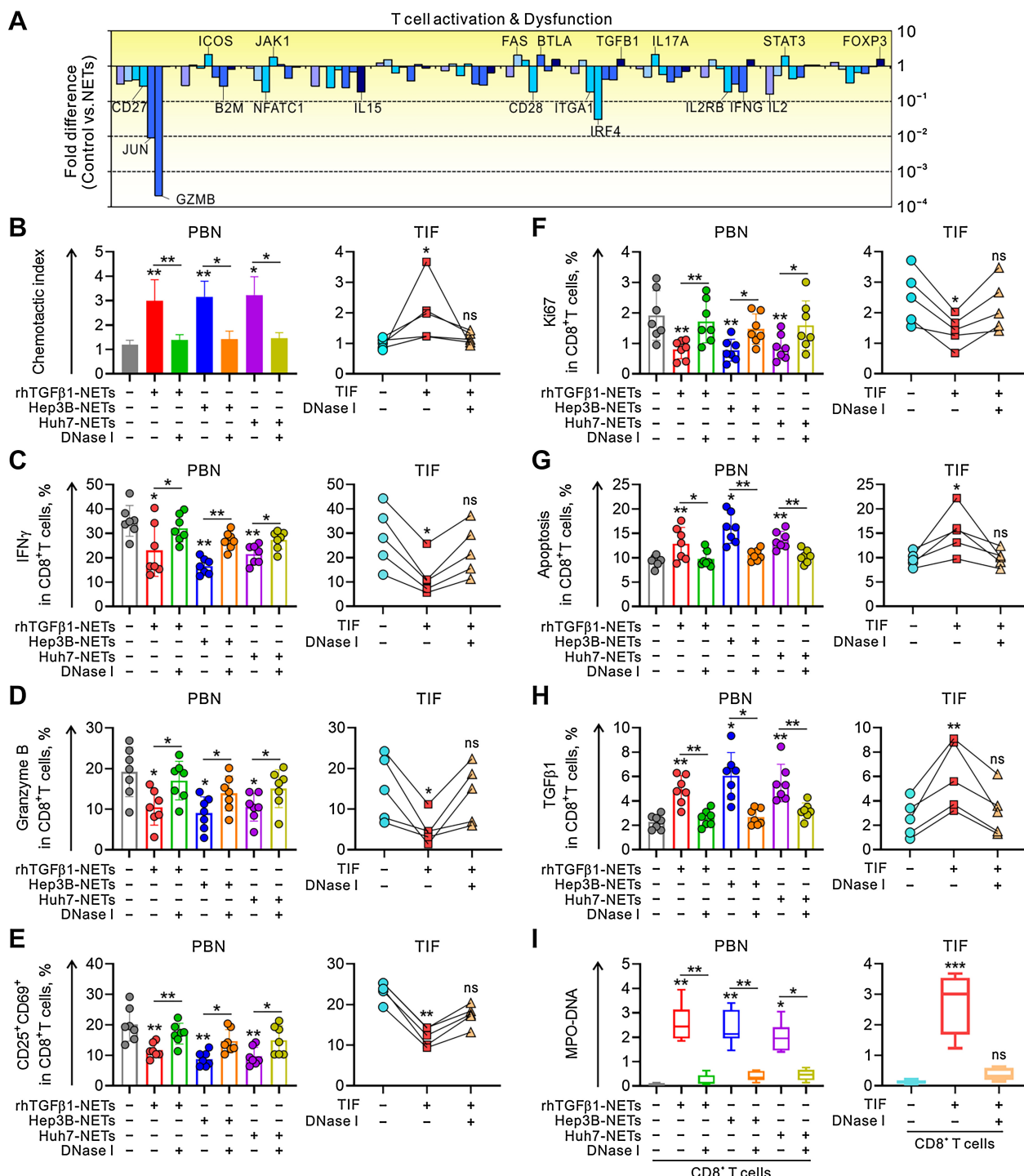
#### **NET-DNA recruits CD8 $^{+}$ T cells and inhibits their cytotoxicity, activation, and survival**

To clarify the direct impact of NETs on CD8 $^{+}$  T cells, human CD8 $^{+}$  T cells were isolated from the PBMCs and then treated with TGF $\beta$ 1-induced NETs *in vitro*. Upon NET stimulation, most of the genes representing T-cell activation, including *GZMB*, *JUN*, *IRF4*, *ITGA1*, *CD28*, *IL15*, *NFATC1*, *IL2*, *IFNG*, *IL2RB*, *B2M*, and *CD27*, were significantly downregulated; in contrast, most of the genes representing T-cell dysfunction, including *ICOS*, *FAS*, *BTLA*, *IL17A*, *STAT3*, *JAK1*, *FOXP3*, and *TGFB1*, were significantly upregulated (**Fig. 3A**). The expression of immune checkpoints was dramatically increased after NET stimulation (Supplementary Fig. S7A). We next induced different kinds of NETs *in vitro* by stimulating human peripheral blood neutrophils (PBN) with rhTGF $\beta$ 1 or coculturing PBNs with TGF $\beta$ 1-expressing HCC cells. These *in vitro*-induced NETs, also termed “PBN-NETs,” were used for the treatment of human CD8 $^{+}$  T cells (Supplementary Fig. S7B). Previous studies revealed NETs as a chemotactic factor to attract pathogens or cancer cells (12). We therefore evaluated their chemotactic effect on CD8 $^{+}$  T cells and found similar results (**Fig. 3B**), which was abrogated by DNase I, an endonuclease that cleaves DNA and is therefore used as a NET inhibitor (25), indicating that the DNA component of NETs play a dominant role in this process. Moreover, CD8 $^{+}$  T cells treated with various PBN-NETs showed concordant lower protein levels of IFN $\gamma$  and granzyme B (**Fig. 3C** and **D**), CD25 and CD69 (**Fig. 3E**), and Ki67 (**Fig. 3F**) but higher protein levels of apoptosis markers (**Fig. 3G**); however, such phenomena were also abolished upon DNase I treatment. These data indicate that NET-DNA can recruit CD8 $^{+}$  T cells, inhibit their cytotoxicity, activation, and proliferation, and induce their apoptosis *in vitro*.

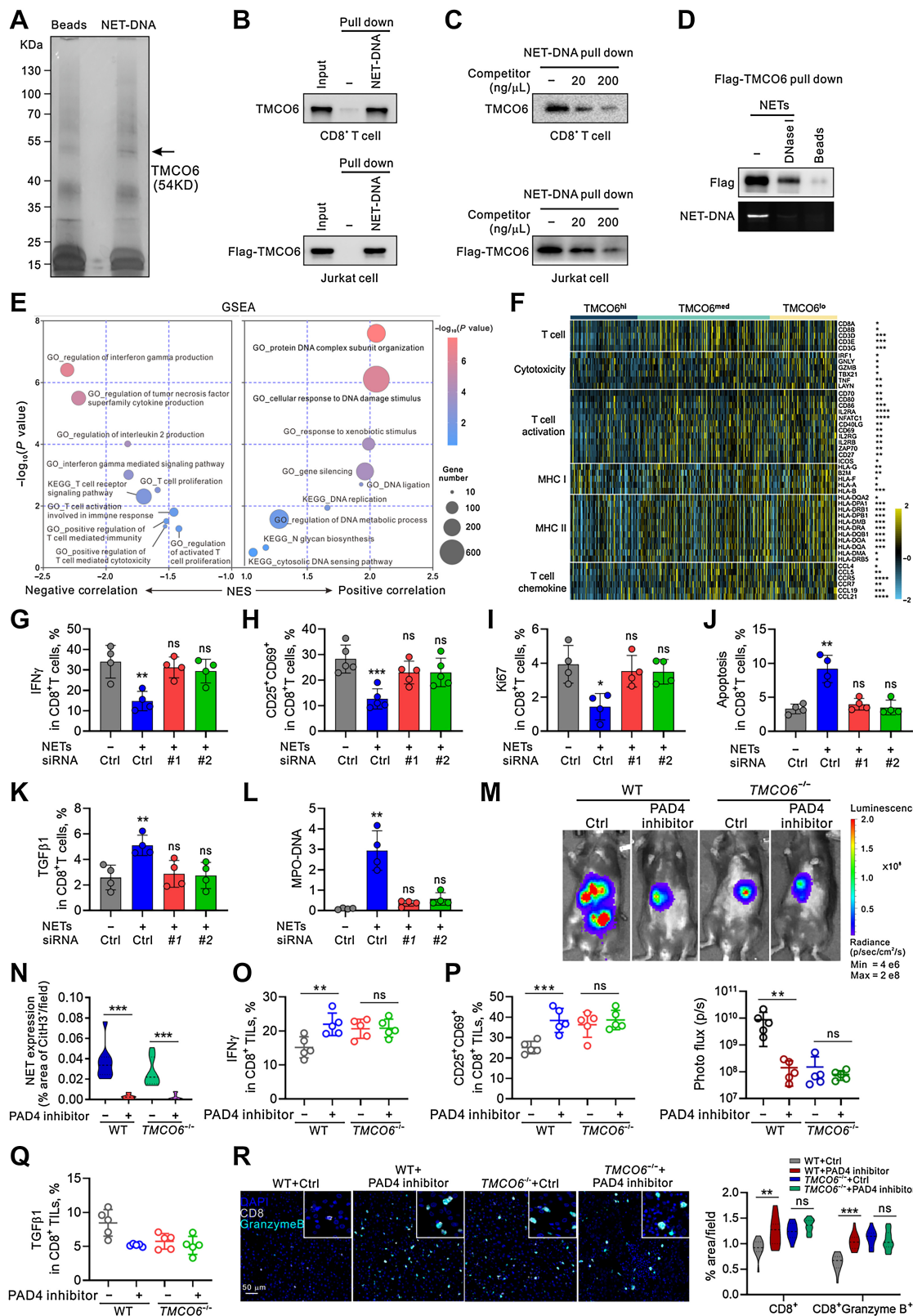
We next investigated the effects of patient-derived NETs on CD8 $^{+}$  T-cell immunity (Supplementary Fig. S7B). TIF isolated from patients with HCC was used for the treatment of CD8 $^{+}$  T cells from the PBMCs of healthy donors. Similarly, more CD8 $^{+}$  T cells were recruited in the presence of TIF (**Fig. 3B**); TIF diminished the cytotoxicity (**Fig. 3C** and **D**), activation (**Fig. 3E**), and proliferation (**Fig. 3F**) of CD8 $^{+}$  T cells but enforced their apoptosis (**Fig. 3G**); all these effects of TIF on CD8 $^{+}$  T cells were attenuated by inhibiting NETs with DNase I. These results further validate the role of NET-DNA in suppressing the CD8 $^{+}$  T-cell response.

#### **NET-DNA-educated CD8 $^{+}$ T cells release more TGF $\beta$ 1 to accelerate the impairment of antitumoral immunity**

Dysfunctional T cells are also characterized by overexpression of multiple immunosuppressive factors (26). We found that the frequency of TGF $\beta$ 1 $^{+}$  CD8 $^{+}$  T cells was dramatically increased after stimulation with PBN-NETs or TIF, whereas DNase I treatment restrained these effects (**Fig. 3H**). Similar results were obtained in the secreted TGF $\beta$ 1 (Supplementary Fig. S7C). In particular, the supernatants of

**Figure 3.**

NET-DNA recruits CD8<sup>+</sup> T cells and inhibits their cytotoxicity, activation, and survival via a positive feedback loop mediated by TGF $\beta$ 1. **A**, Human CD8<sup>+</sup> T cells isolated from the PBMCs of healthy donors were treated with rhTGF $\beta$ 1-induced NETs (5  $\mu$ g/mL) produced by neutrophils from the same donors for 48 hours *in vitro*. PCR array analyses were performed for the expression of gene signatures representing T-cell activation and dysfunction. **B-I**, Human neutrophils isolated from the PBN of healthy donors were stimulated with rhTGF $\beta$ 1 or cocultured with HCC cell lines for 3 hours *in vitro* to induce NETs; these NETs were pretreated with or without DNase I (1 mg/mL) and then used for the treatment of CD8<sup>+</sup> T cells from the PBMC of the same donor (left);  $n = 7$ . TIF isolated from fresh tumor tissues of patients with HCC were pretreated with or without DNase I and then used for the treatment of CD8<sup>+</sup> T cells from the PBMCs of healthy donors (right); TIF, fresh medium = 1:50;  $n = 4$ . CD8<sup>+</sup> T-cell chemotactic assay was performed by adding control medium or medium containing NETs pretreated with or without DNase I into lower chambers (**B**). After 72 hours treatment, flow cytometry analyses for the expression of IFN $\gamma$  (**C**), granzyme B (**D**), CD25 and CD69 (**E**), Ki67 (**F**), apoptotic Annexin V/7AAD (**G**), and TGF $\beta$ 1 (**H**) by CD8<sup>+</sup> T cells. CD8<sup>+</sup> T cells treated under the indicated conditions were replaced with fresh medium and treated for another 72 hours. Supernatants of CD8<sup>+</sup> T cells were collected for naïve neutrophil treatment for 3 hours, and indicated supernatants of neutrophils were collected for the detection of MPO-DNA (**I**). Data are representative of three independent experiments. \*,  $P < 0.05$ ; \*\*,  $P < 0.01$ ; \*\*\*,  $P < 0.001$ , by one-way ANOVA for the multiple comparisons (**B-I**). ns, nonsignificant.



CD8<sup>+</sup> T cells under the abovementioned conditions were collected for further treatment of human neutrophils. We found more NET formation in neutrophils from the groups of CD8<sup>+</sup> T cells treated with PBN-NETs or TIF than those from the CD8<sup>+</sup> T-cell alone groups, which was efficiently reversed through DNase I treatment (Fig. 3I). Overall, we preliminarily surmise that NET-DNA-educated CD8<sup>+</sup> T cells release more TGFβ1 to boost NET production, thus forming a positive feedback loop.

TGFβ1 has been shown to get attached to NETs (27). We found that blocking TGFβ1 did not affect the roles of NETs on CD8<sup>+</sup> T cells (Supplementary Fig. S7D–S7H), suggesting that TGFβ1-induced NETs mainly act on CD8<sup>+</sup> T cells in the form of NETs itself, but not TGFβ1. The effects of NETs induced by other stimulators, such as PMA and LPS (24, 28), on CD8<sup>+</sup> T cells were generally similar to those of TGFβ1-induced NETs (Supplementary Fig. S7I–S7M), indicating that NETs induced by different stimulators may have a consistent effect on CD8<sup>+</sup> T-cell immunity.

#### NET-DNA binds to TMCO6 on CD8<sup>+</sup> T cells and induces their dysfunction

Next, we wondered whether NET-DNA exerted its functions via interaction with a receptor on CD8<sup>+</sup> T cells. NET-DNA was purified and labeled with biotin; membrane proteins were isolated from CD8<sup>+</sup> T cells and then incubated with biotinylated NET-DNA (Supplementary Fig. S8A). Streptavidin magnetic beads coupled with biotinylated NET-DNA pulled down a protein of 54 kDa (Fig. 4A), which was determined as TMCO6 by LC/MS-MS (Supplementary Fig. S8B) and further confirmed by IP assay (Fig. 4B). The specific binding of either endogenous TMCO6 in CD8<sup>+</sup> T cells or flag-TMCO6 in Jurkat cells to biotinylated NET-DNA was also confirmed by competition assay (Fig. 4C). Pretreatment of DNase I (Fig. 4D) but not proteinase K (Supplementary Fig. S8C and S8D) efficiently abolished the binding of NET-DNA to TMCO6, validating the specific interaction between TMCO6 and DNA not protein components of NETs. In addition, NET-DNA can be pulled down by anti-flag beads coupled with Flag-TMCO6 proteins, and no other significant ligands were pulled down (Supplementary Fig. S8E). Together, these data suggest that TMCO6 serves as a specific cell-surface receptor of NET-DNA in CD8<sup>+</sup> T cells.

Neither TMCO6 in CD8<sup>+</sup> T cells nor flag-TMCO6 protein in Jurkat cells was detected in the immunoprecipitates of bacterial double-

stranded DNA (Supplementary Fig. S8F). Bacterial double-stranded DNA had no competitive effect on the interaction of TMCO6 with NET-DNA (Supplementary Fig. S8G), indicating that TMCO6 might serve an exclusive receptor of NET-DNA.

As a newly discovered transmembrane protein, the exact biological function of TMCO6 has not been reported in cancer or other diseases. Gene set enrichment analysis (GSEA) of the HCC data from TCGA dataset indicated a strongly positive correlation between TMCO6 and “protein DNA complex subunit organization” and “cellular response to DNA damage stimulus” (Fig. 4E; Supplementary Fig. S8H). Nevertheless, TMCO6 showed a strongly negative correlation with the regulation of multiple cytotoxic cytokines, including IFNγ, the tumor necrosis factor superfamily and IL2, the T-cell receptor (TCR) signaling pathway, T-cell proliferation, T-cell activation, and T cell-mediated immunity (Fig. 4E). As shown in Fig. 4F, TMCO6-low patients showed a strong enrichment of several immune gene signatures, including T-cell cytotoxicity, T-cell activation, MHC class I and II, and T-cell chemokine. We also found that NET-DNA could upregulate TMCO6 expression on CD8<sup>+</sup> T cells (Supplementary Fig. S8I and S8J). On the basis of these results, we hypothesized that TMCO6 might be essential for NET-DNA-induced impairment of CD8<sup>+</sup> T-cell immunity.

To test this hypothesis, we silenced TMCO6 expression with siRNA in CD8<sup>+</sup> T cells (Supplementary Fig. S8K and S8L). TMCO6 knockdown remarkably restored the decreased cytotoxicity, activation, and proliferation, as well as the enhanced apoptosis, recruitment, TGFβ1 expression, and the effects of TGFβ1 on NET formation (Fig. 4G–L; Supplementary Fig. S8M–S8O) in CD8<sup>+</sup> T cells treated with NETs. These results suggest that NET-DNA regulates CD8<sup>+</sup> T-cell immunity via TMCO6.

Next, a syngeneic orthotopic HCC model was constructed in WT C57BL/6 and TMCO6-deficient (*TMCO6*<sup>-/-</sup>) mice (Fig. 4M). There was no significant difference for the phenotypes of CD8<sup>+</sup> T, CD4<sup>+</sup> T, and NK cells between WT and *TMCO6*<sup>-/-</sup> mice (Supplementary Fig. S8P–S8R). The presence of NETs was observed in *TMCO6*<sup>-/-</sup> mice, with slightly lower levels than those in WT, which was blocked by PAD4 inhibitor (Fig. 4N; Supplementary Fig. S9A and S9B). PAD4 inhibition showed potent antitumor effect in WT mice but not *TMCO6*<sup>-/-</sup> mice (Fig. 4M). Compared with WT mice, the effects of PAD4 inhibitor on CD8<sup>+</sup> TILs were also restricted in *TMCO6*<sup>-/-</sup>

**Figure 4.**

NET-DNA binds to TMCO6 on CD8<sup>+</sup> T cells and induces their dysfunction. **A**, Biotinylated NET-DNA pulldown assay in CD8<sup>+</sup> T cells. **B**, NET-DNA pulldown assay for the membrane proteins of human CD8<sup>+</sup> T cells from the PBMCs pulled down by biotinylated NET-DNA by using anti-TMCO6 antibody (top) and for the membrane proteins of Jurkat cells transfected with flag-TMCO6 plasmids pulled down by biotinylated NET-DNA by using anti-flag antibody (bottom). **C**, NET-DNA pulldown assay for the specific binding of endogenous TMCO6 in human CD8<sup>+</sup> T cells (top) or flag-TMCO6 in Jurkat cells transfected with flag-TMCO6 plasmids (bottom) to biotinylated NET-DNA in the absence or in the presence of increasing concentrations of the competitor, unlabeled NET-DNA. **D**, Flag-TMCO6 protein in Jurkat cells transfected with flag-TMCO6 plasmids was purified. NETs were pretreated with (middle) or without (left) DNase I, coupled to specific DNA-binding beads, and then incubated with Flag-TMCO6. The interaction of NETs and TMCO6 was assessed by the IP of NETs-beads and blotted with anti-Flag antibody. Flag-TMCO6 mixed with empty beads without DNA served as a negative control (right). The digestion efficiency of NET-DNA by DNase I was validated by agarose gel analysis for DNA. **E**, GSEA was conducted to identify the top significant GO terms and Kyoto Encyclopedia of Genes and Genomes (KEGG) pathways correlated with *TMCO6* in TCGA dataset of HCC. **F**, Heat map representation of the gene clusters based on TCGA dataset of HCC. *TMCO6*<sup>high</sup>, *TMCO6*<sup>high</sup>, *TMCO6*<sup>med</sup>, *TMCO6*<sup>medium</sup>, *TMCO6*<sup>lo</sup>, *TMCO6*<sup>low</sup>. **G–L**, Human CD8<sup>+</sup> T cells were transfected with siControl, si*TMCO6*#1, or si*TMCO6*#2 RNA following NETs (5 µg/mL) treatment for 72 hours. Flow cytometry analysis for the expression of indicated markers (G–K). CD8<sup>+</sup> T cells treated under the indicated conditions were replaced with fresh medium and treated for another 72 hours. Supernatants of CD8<sup>+</sup> T cells were collected for naïve neutrophil treatment for 3 hours, and indicated supernatants of neutrophils were collected for the detection of MPO-DNA (L). **M–R**, WT or *TMCO6*<sup>-/-</sup> C57BL/6 tumor-bearing mice were treated with or without PAD4 inhibitor, Cl-amidine (10 mg/kg/day, intraperitoneally). Tumor growth was measured using an *in vivo* imaging system at 4 weeks after tumor implantation (M). Cith3-positive areas representing NET expression in tumors are shown as a statistical graph (N). Flow cytometry analysis for the expression of indicated markers by CD8<sup>+</sup> TILs infiltrated in the orthotopic mouse tumors (O–Q). Representative photomicrographs of IF staining for the colocalization of CD8 (white), granzyme B (cyan), and DAPI (blue) in tested mouse tumors. Scale bars, 50 µm. CD8-positive areas and CD8 and granzyme B double-positive areas are shown as statistical graphs (R). Data are representative of three independent experiments. \*, *P* < 0.05; \*\*, *P* < 0.01; \*\*\*, *P* < 0.001, by one-way ANOVA for the multiple comparisons (G–L and N–R). ns, nonsignificant.

mice, including the infiltration number, cytotoxicity, activation, proliferation, apoptosis, and expression of TGF $\beta$ 1 and PD-1 (**Fig. 4O–R**; Supplementary Fig. S9C–S9F). However, PAD4 inhibition had no effect on CD8 $^{+}$  T and NK cells (Supplementary Fig. S9G and S9H). These data indicate that blocking NET production by PAD4 inhibitor alleviates the exhausted status of CD8 $^{+}$  T cells and enhances their activation and effector function *in vivo*, which is mediated by TMCO6.

Next, we adoptively transferred CD45.2 $^{+}$  CD8 $^{+}$  T cells from WT or TMCO6 $^{-/-}$  mice into CD45.1 tumor-bearing mice. TMCO6 KO remarkably increased the activation, proliferation, and cytotoxicity of tumor-infiltrating CD45.2 $^{+}$  CD8 $^{+}$  T cells, but decreased their apoptosis and expression of immunosuppressive TGF $\beta$ 1 and PD-1 (Supplementary Fig. S9I). Notably, we clearly observed the physical engagement of NETs with TMCO6-expressing CD45.2 $^{+}$  CD8 $^{+}$  T cells within the TME (Supplementary Fig. S9J). These data substantiate the role of TMCO6 in CD8 $^{+}$  T cells interacting with NETs during HCC progression.

#### The transmembrane protein TMCO6 interacts with NET-DNA at its N-terminus and inhibits the activation of TCR signaling pathway and the nuclear translocation of NF $\kappa$ B p65

To ascertain how TMCO6 binds to NET-DNA, we searched the Alliance of Genome Resources website (<https://www.alliancegenome.org/>) and the ProtScale website (<https://www.expasy.org/resources/protscale>), and TMCO6 was predicted to be an integral component of the membrane and a transmembrane protein with two transmembrane regions, a hydrophobicity score greater than 0, and a hydrophilicity score of 0.118 (Supplementary Fig. S9K). TMCO6 with a Flag tag at the N-terminus was detected in both surface and intracellular staining, while TMCO6 with a Flag tag at the C-terminus was detected only in permeable staining (**Fig. 5A**), suggesting that TMCO6 may be a transmembrane protein consisting of an extracellular N-terminus and an intracellular C-terminus. Indeed, we clearly observed the extracellular location of TMCO6 with a Flag tag at the N-terminus and the intracellular location of TMCO6 with a Flag tag at the C-terminus (**Fig. 5B**). To further determine the regions of TMCO6 interacting with NET-DNA, we constructed TMCO6 truncations by deleting 80 amino acids at its C-terminus or N-terminus (**Fig. 5C**). An *in vitro* NET-DNA pulldown assay revealed that the N-terminal but not C-terminal region of TMCO6 bound to NET-DNA (**Fig. 5D**). Consistently, the colocalization of NET-DNA with TMCO6 was completely abrogated once the N-terminal region of TMCO6 was truncated (**Fig. 5E**). These results indicate that the transmembrane protein TMCO6 interacts with NET-DNA at its N-terminus.

GSEA indicated a significantly negative correlation between TMCO6 and the TCR signaling pathway and regulation of NF $\kappa$ B import into the nucleus (**Figs. 4E** and **5F**). NET treatment significantly inhibited the activation of TCR signaling, including phospho-Scr, phospho-Zap70, phospho-SLP-76, and phospho-PLC $\gamma$ 1 in cells with full-length TMCO6, which were abrogated in cells with N-terminus-truncated TMCO6 (**Fig. 5G**). Similar results were found in the nuclear translocation of NF $\kappa$ B p65 (**Fig. 5H** and **I**). Consistently, the effects of NET-TMCO6 on T-cell signaling were further confirmed in primary CD8 $^{+}$  T cells (Supplementary Fig. S9L and S9M). Collectively, these data suggest that the N-terminus of TMCO6 binds to NET-DNA and then suppresses the activation of the TCR signaling pathway and the nuclear translocation of NF $\kappa$ B p65.

Upon inhibition of NF $\kappa$ B *in vitro*, NET treatment had an influence on the cytotoxicity, activation, proliferation, apoptosis, and TGF $\beta$ 1

expression in control (**Fig. 5J** and **K**) or TMCO6-silenced CD8 $^{+}$  T cells (Supplementary Fig. S9N), indicating that inhibition of NF $\kappa$ B pathway is responsible for CD8 $^{+}$  T-cell dysfunction mediated by the NET-TMCO6 axis.

#### TGF $\beta$ 1 signaling inhibition and anti-PD-1 effectively inhibit HCC progression in mice

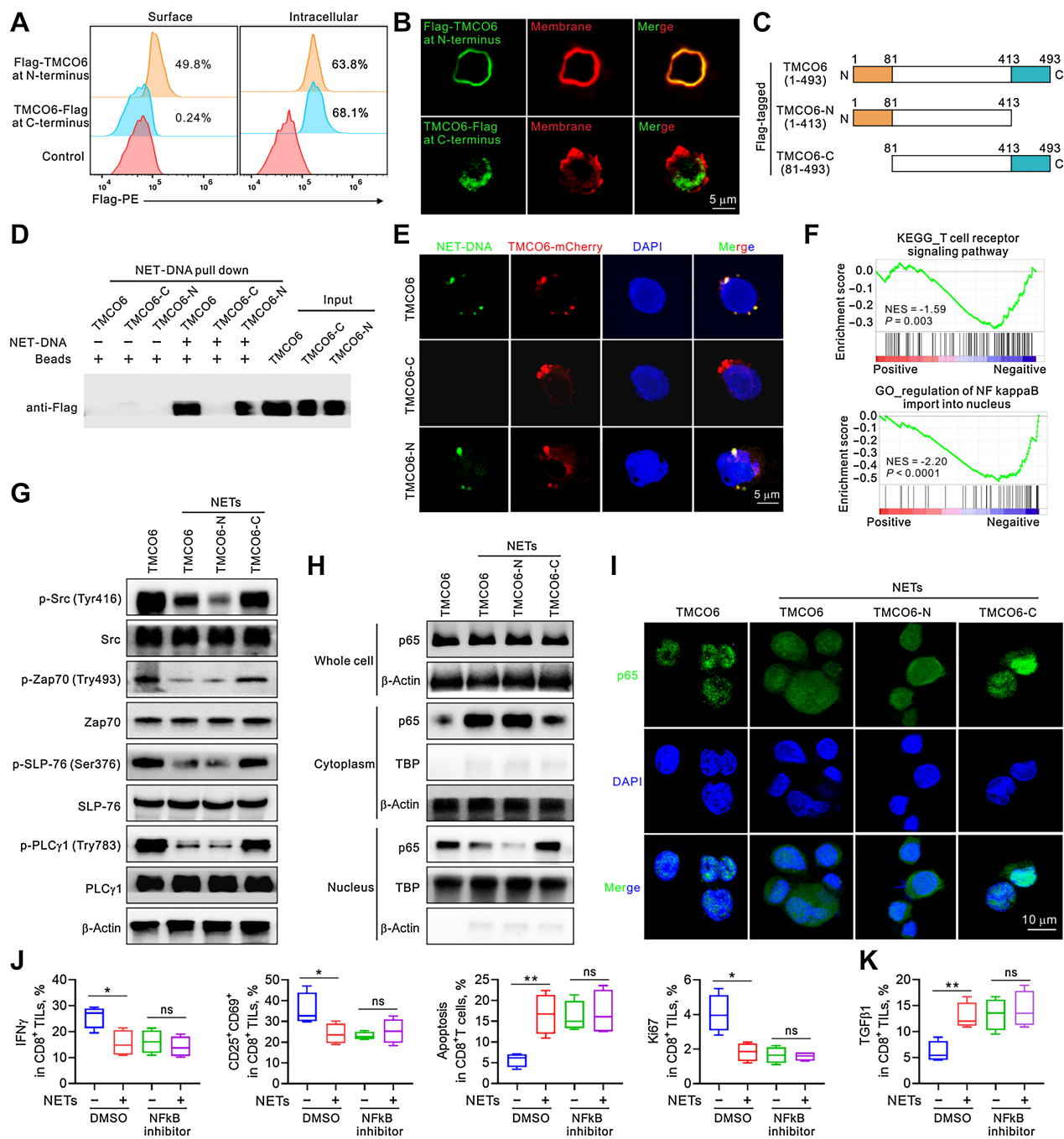
We next explored the therapeutic effect of TGF $\beta$ 1 signaling inhibition with galunisertib, a novel TGF $\beta$ 1 receptor type I inhibitor (29), and its combination with anti-PD-1 *in vivo* (**Fig. 6A**). The administration of galunisertib and anti-PD-1 led to a more significant delay in tumor progression (**Fig. 6B** and **C**) and a more prolonged survival (**Fig. 6D**) than galunisertib or anti-PD-1 alone. NETs were strongly inhibited by galunisertib treatment (Supplementary Fig. S10A and S10B). CD8 $^{+}$  TILs in mice treated with galunisertib and anti-PD-1 had significantly increased expression of IFN $\gamma$  compared with those in mice treated with IgG, galunisertib alone, or anti-PD-1 antibody alone (**Fig. 6E**). Furthermore, the exhaustion status of CD8 $^{+}$  TILs in mouse tumors was also relieved, as shown by decreased levels of TIM3 and LAG3 (**Fig. 6F**). Consistent results were observed for the infiltration of CD8 $^{+}$  T cells and their expression of granzyme B in mouse tumors (Supplementary Fig. S10C). These data suggest that galunisertib and anti-PD-1 effectively blocked NET-mediated tumor progression *in vivo*.

#### Targeting TMCO6 improves anti-PD-1 efficacy in mice

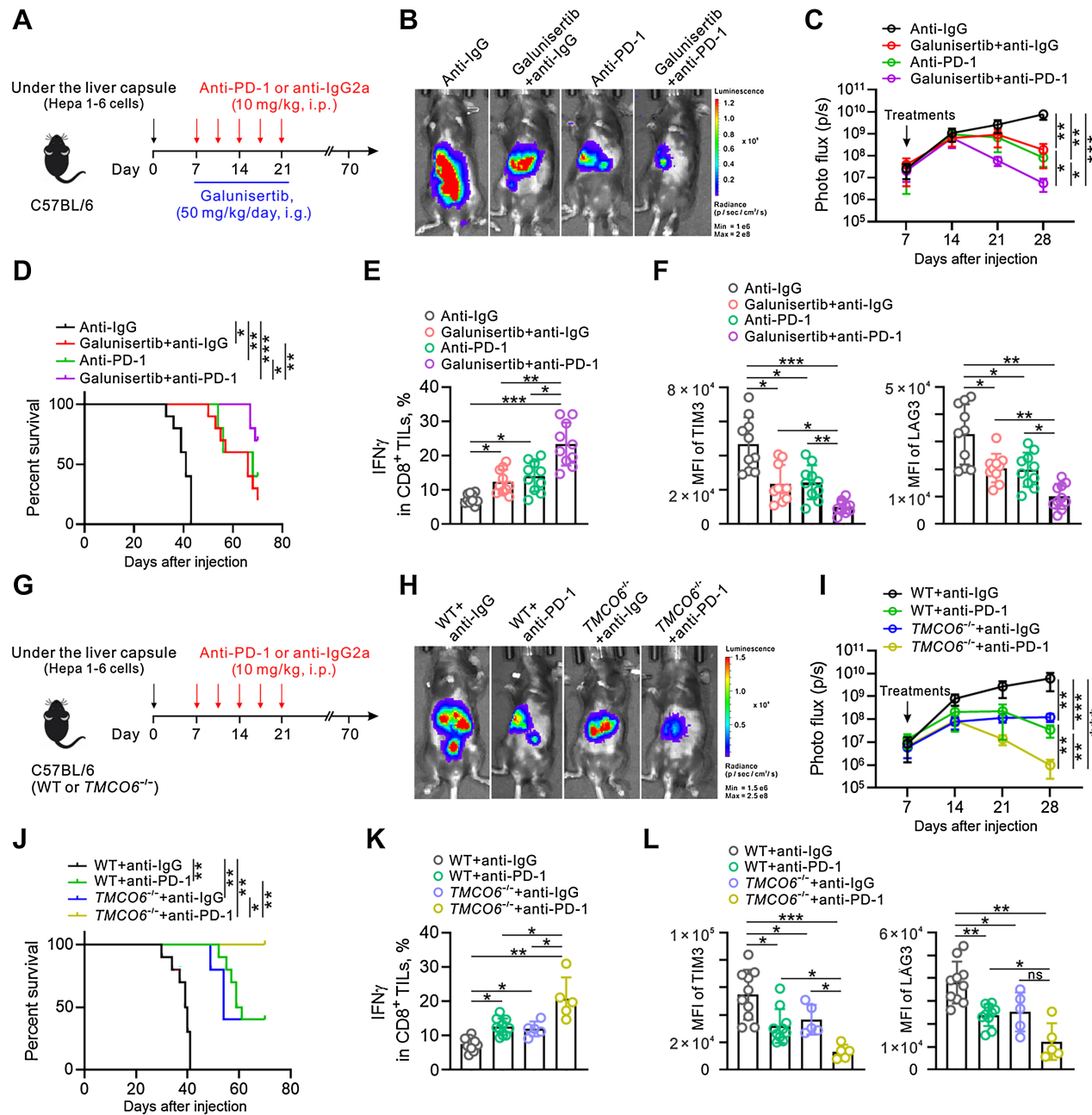
Another orthotopic HCC model was designed to investigate the therapeutic effect of TMCO6 deficiency in combination with anti-PD-1 (**Fig. 6G**). TMCO6 $^{-/-}$  mice exhibited retarded tumor progression than WT mice, and TMCO6 $^{-/-}$  mice with anti-PD-1 treatment had the most dramatic tumor regression (**Fig. 6H** and **I**), improved survival (**Fig. 6J**), as well as decreased NET expression (Supplementary Fig. S10D and S10E) compared with mice in the other three groups. The concentration of TGF $\beta$ 1 in TIF was in line with the expression level of NETs (Supplementary Fig. S10F). CD8 $^{+}$  TILs in TMCO6 $^{-/-}$  mice displayed higher expression of IFN $\gamma$  (**Fig. 6K**) and lower expression of TIM3 and LAG3 (**Fig. 6L**) than those in WT mice; moreover, such effects were further enforced upon anti-PD-1 treatment. CD8 $^{+}$  T-cell infiltration was significantly increased in tumors of TMCO6 $^{-/-}$  mice with anti-PD-1 treatment, and the expression of granzyme B was also markedly increased (Supplementary Fig. S10G). Collectively, our findings suggest that TMCO6 deficiency enhances anti-PD-1 efficacy, and their combination effectively inhibits NET-driven tumor progression and restores CD8 $^{+}$  T-cell immunity.

#### scRNA-seq analysis reveals an exhausted phenotype of the TMCO6-positive CD8 $^{+}$ T-cell subset in patients with HCC

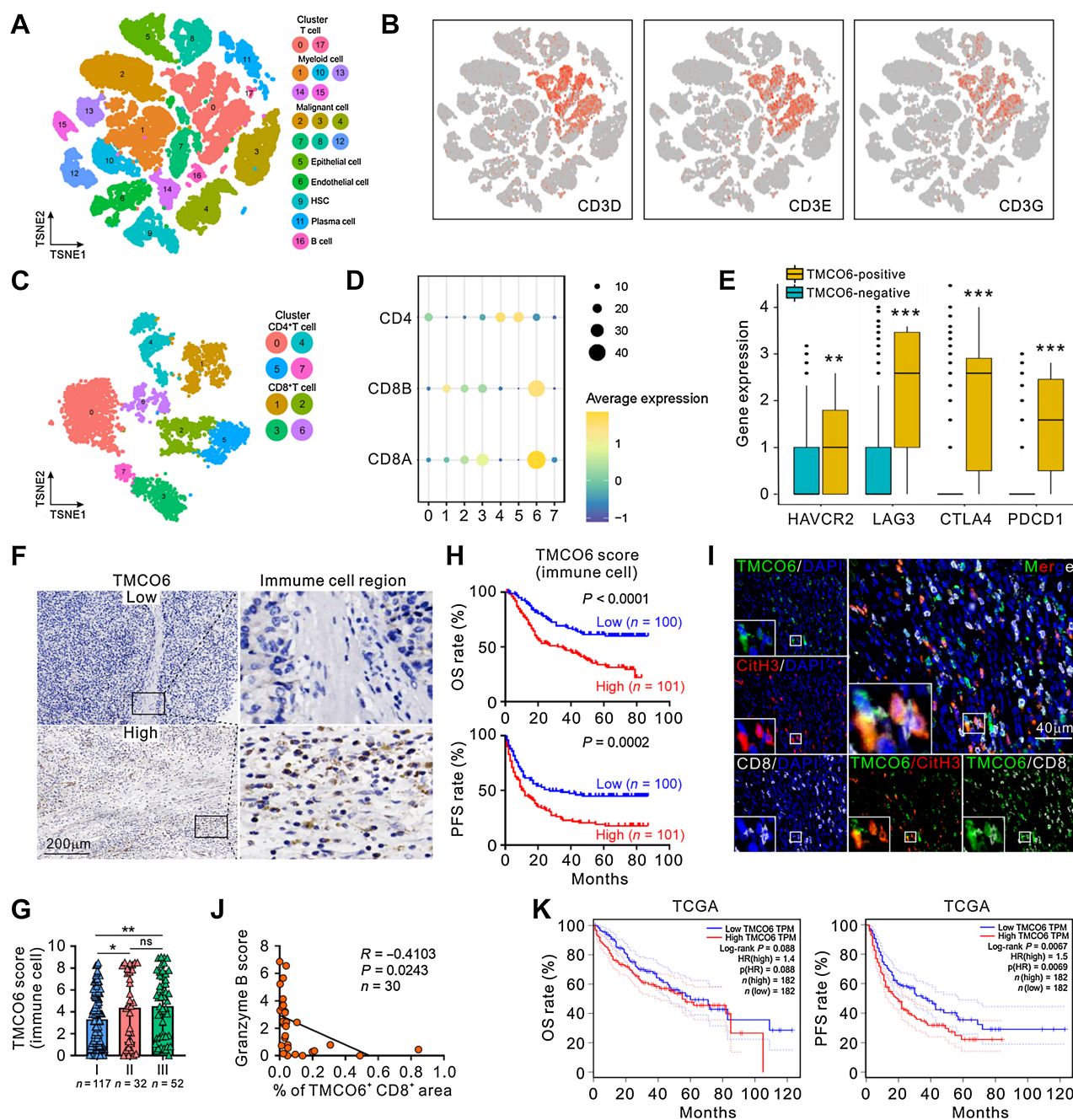
We performed scRNA-seq analysis based on a single-cell atlas of the multicellular ecosystem of HCC generated in a recent study. We selected the clustering resolution (0.1) that separated the cells into 18 clusters (**Fig. 7A**). Then, CD3 $^{+}$  T-cell signatures were visualized to identify the expression of lymphoid cell clusters (cluster 0 and 17; **Fig. 7B**). We further selected the clustering resolution (0.3) that separated the CD3 $^{+}$  T cell into eight clusters (**Fig. 7C**). T-cell marker genes were visualized using the bubble chart (**Fig. 7D**). Compared with the TMCO6-negative CD8 $^{+}$  T-cell cluster, the TMCO6-positive cluster showed elevated expression levels of checkpoints, including HAVCR2, LGA3, CTLA4, and PDCD1 (**Fig. 7E**). Such observations indicate that TMCO6-positive CD8 $^{+}$  T cells show an exhaustion status.

**Figure 5.**

The transmembrane protein TMCO6 interacts with NET-DNA at its N-terminus and inhibits the activation of TCR signaling and the nuclear translocation of p65. **A** and **B**, Jurkat cells were transfected with full-length TMCO6 tagged with Flag at the N-terminus (Flag-TMCO6) or C-terminus (TMCO6-Flag). Flow cytometry analysis for Flag signal by surface and intracellular staining (**A**). Representative photomicrographs of IF staining for the colocalization of Flag-TMCO6 or TMCO6-Flag with the cytoplasmic membrane. TMCO6 was stained with anti-Flag (green), and cytoplasmic membrane was stained with Dil (red; **B**). Scale bars, 5 μm. **C**, Schematics of TMCO6 truncations. **D**, Jurkat cells were transfected with Flag-tagged full-length or truncated TMCO6. IP assay was performed for the membrane proteins pulled down by NET-DNA by using anti-flag antibody. **E**, Jurkat cells were transfected with mCherry-tagged full-length or truncated TMCO6 and then incubated with NET-DNA stained with SYTOX Green. Representative confocal microscopy images showing the colocalization of NET-DNA (green) and TMCO6 (red). **F**, GSEA plot showed a significantly negative correlation of TMCO6 with “KEGG\_TCR signaling pathway” and gene ontology term of “regulation of NFκB import into nucleus” in TCGA database of HCC. **G-I**, Jurkat cells transfected with Flag-tagged full-length TMCO6 or truncated TMCO6 were treated with or without NETs (5 μg/mL) for 72 hours. Western blot analysis for their phosphorylated and total expression of Src, Zap70, SLP-76, and PLCγ1 (**G**). Western blot analysis for p65 expression in whole cell, cytoplasm, and nucleus (**H**). Immunofluorescent staining for the cellular location of p65 (**I**). **J** and **K**, Human CD8<sup>+</sup> T cells were pretreated with DMSO or NFκB inhibitor, QNZ (EVP4593, 20 μmol/L) for 1 hour, following treatment with or without NETs (5 μg/mL) for 72 hours. Flow cytometry analysis for the expression of indicated markers. *n* = 4. Data are representative of three independent experiments. \*, *P* < 0.05; \*\*, *P* < 0.01, by one-way ANOVA for the multiple comparisons (**J** and **K**). ns, nonsignificant.

**Figure 6.**

Combination therapy of TGF $\beta$ 1 signaling inhibition or TMCO6 deficiency and anti-PD-1 inhibits HCC progression in mouse models. **A**, Experimental scheme illustrating the treatment plan for the orthotopic HCC model in C57BL/6 mice.  $n = 10$  for each group. **B**, Tumor growth for the mice in **A** was measured using an *in vivo* imaging system at 4 weeks after tumor implantation. **C**, Photo flux of tumor growth for the mice in **A** at different time points. **D**, Kaplan-Meier survival curves for the mice in **A**. **E** and **F**, Flow cytometry analysis for the expression of indicated markers by CD8 $^{+}$  TILs infiltrated in the orthotopic mouse tumors in **A**. **G**, Experimental scheme illustrating the treatment plan for the orthotopic HCC model in WT or TMCO6 $^{-/-}$  C57BL/6 mice.  $n = 10$  for WT mice treated with anti-IgG or anti-PD-1;  $n = 5$  for TMCO6 $^{-/-}$  mice treated with anti-IgG or anti-PD-1. **H**, Tumor growth for the mice in **G** was measured using an *in vivo* imaging system at 4 weeks after tumor implantation. **I**, Photo flux of tumor growth for the mice in **G** at different time points. **J**, Kaplan-Meier survival curves for the mice in **G**. **K** and **L**, Flow cytometry analysis for the expression of indicated markers by CD8 $^{+}$  TILs infiltrated in the orthotopic mouse tumors in **I**. i.p., intraperitoneally; i.g., intragastrically. MFI, mean fluorescence intensity. Data are representative of three independent experiments. \*,  $P < 0.05$ ; \*\*,  $P < 0.01$ ; \*\*\*,  $P < 0.001$ , by one-way ANOVA for the multiple comparisons (**C**, **E**, **F**, **I**, **K**, and **L**) or log-rank test (**D** and **J**). ns, nonsignificant.

**Figure 7.**

TMCO6 expression marks an exhausted status of CD8<sup>+</sup> T cells and associates with poor prognosis in patients with HCC. **A–E**, scRNA-seq analysis for tumor tissues of patients with HCC. **A**, The t-distributed stochastic neighbor embedding (tSNE) plot of 18 cell clusters from the multicellular ecosystem of 10 patients with HCC. Cluster 0 and 17: T cell; cluster 1, 10, and 13–15: myeloid cell; cluster 2–4, 8, and 12: malignant cell; cluster 5: epithelial cell; cluster 6, endothelial cell; cluster 9: HSC; cluster 11: plasma cell; cluster 14: B cell. **B**, The tSNE plots showing the expression levels of signature genes of CD3<sup>+</sup> T cell types. **C**, The tSNE plot of eight cell clusters from the CD8<sup>+</sup> T-cell types. Cluster 0, 4, 5, and 7: CD4<sup>+</sup> T cell; cluster 1–3 and 6: CD8<sup>+</sup> T cell. **D**, The marker genes expression patterns of signature genes in T cell. **E**, Expression differences of T-cell exhaustion genes between TMCO6-positive and TMCO6-negative CD8<sup>+</sup> T cell groups. **F**, Representative photomicrographs of IHC staining for the low and high expression of TMCO6 in primary tumor tissues from patients with HCC. Scale bar, 200 μm. **G**, TMCO6 stained in immune cell region in HCC tissues from different stages. **H**, Kaplan-Meier curves for OS and PFS in patients with HCC with low and high TMCO6 expression in immune cell region. **I**, Representative photomicrographs of IF staining for the coexpression pattern of TMCO6 (green), CitH3 (red), CD8 (white), and DAPI (blue) in primary tumor tissues from patients with advanced HCC. Scale bars, 40 μm. CitH3-positive areas representing NETs expression. **J**, Correlation between granzyme B score in IHC staining and the double-positive areas of TMCO6 (green) and CD8 (white) in IF staining were analyzed in 30 HCC tissues. **K**, Kaplan-Meier curves for OS and PFS in patients with HCC with low and high TMCO6 expression in TCGA online database ( $n = 364$ ). HSC, hepatic stellate cell. Data in **F–J** are representative of three independent experiments. \*,  $P < 0.05$ ; \*\*,  $P < 0.01$ ; \*\*\*\*,  $P < 0.0001$ , by Wilcoxon-Mann-Whitney test (**E**), log-rank test (**H** and **K**), one-way ANOVA for the multiple comparisons (**G**) or Pearson correlation analysis (**J**). ns, nonsignificant.

### High TMCO6 expression by immune cells is correlated with poor prognosis in patients with HCC

In human HCC tissues, TMCO6 was stained in both the immune cell (**Fig. 7F**) and tumor cell (Supplementary Fig. S11A) regions. Patients with stage II and III had a higher expression level of TMCO6 in the immune cell region than those without stage I (**Fig. 7G**), which was closely correlated with reduced long-term survival (**Fig. 7H**). Moreover, we observed clear staining of membrane TMCO6 on CD8<sup>+</sup> T cells in advanced HCC tissues, which was physically adjacent to NET-deposited CitH3 (**Fig. 7I**). The expression of TMCO6 on CD8<sup>+</sup> T cells showed a negative association with granzyme B (**Fig. 7J**; Supplementary Fig. S11B).

In addition, TMCO6 expressed by tumor cells had no association with tumor stage (Supplementary Fig. S11C) or patient survival (Supplementary Fig. S11D). Neither knockdown nor overexpression of TMCO6 in HCC cells affected their proliferation or invasion in the presence or absence of NETs *in vitro* (Supplementary Fig. S11E–I).

### High levels of NET-TMCO6 axis are associated with poor CD8<sup>+</sup> T-cell immunity and poor prognosis in patients with HB

In pancancer analysis, liver cancer showed high expression levels of TMCO6 (Supplementary Fig. S12A), as well as a strong association between high TMCO6 and poor survival in HCC (**Fig. 7K**; Supplementary Fig. S12B–S12J). Subsequently, we performed further analysis on another liver cancer, HB, the most common pediatric liver cancer. Similar to HCC, NETs mainly accumulated in advanced HB (Supplementary Fig. S13A and S13B), associated with poor prognosis (Supplementary Fig. S13C and S13D), and predict survival (Supplementary Fig. S13E and S13F). A TMCO6 expression pattern similar to HCC was also found in HB (Supplementary Fig. S14A). High expression levels of TMCO6 by immune cells were observed in advanced HB and correlated with poor prognosis (Supplementary Fig. S14B and S14C). TMCO6 coexpressed with CD8 was adjacent to NET-deposited CitH3 in advanced HB tissues, and the coexpression level of TMCO6 and CD8 was negatively associated with granzyme B (Supplementary Fig. S14D–S14F). However, TMCO6 expressed by tumor cells had no clinical relevance to tumor stage (Supplementary Fig. S15A) or survival (Supplementary Fig. S15B) and did not influence tumor cell proliferation or invasion in the absence (Supplementary Fig. S15C–S15E) or presence (Supplementary Fig. S15F and S15G) of NETs.

## Discussion

This study reveals the role of NET-DNA in suppressing CD8<sup>+</sup> T-cell immunity. In line with other studies (11, 30), we found that NET-DNA functions as a chemotactic factor to recruit CD8<sup>+</sup> T cells. Meanwhile, higher apoptosis of CD8<sup>+</sup> T cells was observed in the presence of NETs in this study. T cells undergo apoptosis once trapped within NET chromatin during virus infection (31). Therefore, we consider that the less CD8<sup>+</sup> T cells in NET-enriched tumors of mice and patients with HCC may be due to the fact that *in vivo* NETs were also going to induce more CD8<sup>+</sup> T cells apoptosis while recruiting CD8<sup>+</sup> T cells.

Emerging evidence has demonstrated an immunosuppressive role of NETs by acting on other immune cells, for instance, promoting the differentiation of regulatory T cells (17) or creating a physical barrier preventing tumor–cytotoxic cell interactions (15). Naturally, we cannot exclude the regulatory effects of NETs on other immune cells in HCC. We found that PAD4 inhibition reduced tumor progression and NET formation in different mouse models of HCC. However, PAD4 directly affects the activation of tumor-associated macrophages and regulates macrophage-related inflammatory responses, thereby

promoting tumor progression (32). For tumor cells, PAD4 was reported to participate in the induction of epithelial–mesenchymal transition (33); PDA4 also promotes the proliferation, adhesion, migration, or invasion of tumor cells via mitochondrial biogenesis (14) or TLR9-dependent signaling (34). In addition to eliminating NETs, it cannot be excluded that PAD4 inhibition exerts its anti-tumor effect through other biological functions.

Meanwhile, we showed that TGF $\beta$ 1 was an important inducer of NETs, and that targeting TGF $\beta$ 1 signaling with galunisertib in combination with anti-PD-1 effectively rescues NET-DNA-mediated CD8<sup>+</sup> T-cell dysfunction. However, TGF $\beta$ 1 is well described to have direct immunosuppressive effects, such as inhibiting lymphocyte proliferation and activation (35). It is possible that the effects of galunisertib on CD8<sup>+</sup> T cell and tumor growth were caused by inhibition of both TGF $\beta$ 1 and TGF $\beta$ 1-induced NETs. A recent study showed that NETs can activate latent TGF $\beta$ 1 into active form, and this phenomenon might also amplify the loop in this study (27). We found decreased NET levels in TMCO6<sup>-/-</sup> mice treated with anti-PD-1, which might be because the CD8<sup>+</sup> T cells of these mice were functional restored and secreted reduced levels of TGF $\beta$ 1.

TMCO6 is a novel transmembrane protein. Our study identified TMCO6 on the membrane of CD8<sup>+</sup> T cells as a specific receptor of NET-DNA and might be a promising immunotherapeutic target for HCC. Although we did not observe severe adverse effects in mice, TMCO6 should be carefully targeted because its physiologic function in normal tissues is still uncertain. Our findings need to be further verified in a larger number of mice, especially those with CD8<sup>+</sup> T-cell conditional TMCO6 deficiency. Besides, it has been shown that NETs in a variety of human solid tumors are associated to areas to CD8<sup>+</sup> T-cell depletion (36). Consistently, we found fewer CD8<sup>+</sup> T-cell infiltration in NET-enriched tumors of mice and patients. Our study showed that CD8<sup>+</sup> T cells were going to apoptosis in the presence of NETs, which was abolished after inhibiting TMCO6 expression. We also clearly observed that TMCO6 on the membrane of CD8<sup>+</sup> T cells was physically adjacent to NETs in human HCC tissues. Hence, it is possible that TMCO6 ligation elicits CD8<sup>+</sup> T-cell apoptosis mediated by NETs.

In summary, this study uncovers the role of NETs on CD8<sup>+</sup> T-cell immunity in HCC and identifies TMCO6 as a novel NET-DNA receptor on CD8<sup>+</sup> T cells. NET-DNA binds to TMCO6 and induces CD8<sup>+</sup> T-cell dysfunction via suppressing TCR signaling and NF $\kappa$ B p65 nuclear translocation, leading to HCC progression. Inhibiting NET formation or TMCO6 expression improves CD8<sup>+</sup> T-cell function, impairs tumor progression, which is more effective when combined with anti-PD-1. Our findings support NETs as a potential prognostic biomarker and TGF $\beta$ 1-NET-TMCO6 axis as promising immunotherapeutic targets to inhibit HCC progression.

### Authors' Disclosures

No disclosures were reported.

### Authors' Contributions

**M. Song:** Conceptualization, data curation, funding acquisition, investigation, methodology, writing—original draft, writing—review and editing. **C. Zhang:** Software, formal analysis, visualization, methodology. **S. Cheng:** Resources, data curation, formal analysis, visualization, methodology. **D. Ouyang:** Data curation, validation, visualization, methodology. **Y. Ping:** Conceptualization, writing—review and editing. **J. Yang:** Data curation, software, formal analysis, validation. **Y. Zhang:** Resources, formal analysis. **Y. Tang:** Data curation, software, investigation, visualization. **H. Chen:** Data curation, formal analysis, investigation, visualization, methodology. **Q.-j. Wang:** Resources, data curation, formal analysis. **Y.-q. Li:** Validation,

investigation. **J. He:** Validation, methodology. **T. Xiang:** Conceptualization, supervision, project administration, writing—review and editing. **Y. Zhang:** Resources, supervision, funding acquisition. **J.-C. Xia:** Conceptualization, supervision, project administration, writing—review and editing.

## Acknowledgments

The authors express their sincere appreciation for the shared data obtained from the database of TCGA and Gene Expression Omnibus. This study was supported by the National Key Research and Development Program of China (grant no. 2022YFC2705005 to Y. Zhang), the National Scientific Foundation of China (grant no. 82203754 to M. Song), China Postdoctoral Innovation Talents

Support Program (grant no. BX20220364 to M. Song), China Postdoctoral Science Foundation (grant no. 2022M713606 to M. Song), and Basic and Applied Basic Research Project of Guangzhou, Guangdong province, China (grant no. 2023A04J1770 to M. Song).

## Note

Supplementary data for this article are available at Cancer Research Online (<http://cancerres.acrjournals.org/>).

Received September 27, 2023; revised December 7, 2023; accepted February 16, 2024; published first February 21, 2024.

## References

- Geh D, Leslie J, Rumney R, Reeves HL, Bird TG, Mann DA. Neutrophils as potential therapeutic targets in hepatocellular carcinoma. *Nat Rev Gastroenterol Hepatol* 2022;19:257–73.
- Song M, He J, Pan QZ, Yang J, Zhao J, Zhang YJ, et al. Cancer-associated fibroblast-mediated cellular crosstalk supports hepatocellular carcinoma progression. *Hepatology* 2021;73:1717–35.
- Xue R, Zhang Q, Cao Q, Kong R, Xiang X, Liu H, et al. Liver tumour immune microenvironment subtypes and neutrophil heterogeneity. *Nature* 2022;612:141–7.
- Zhou SL, Yin D, Hu ZQ, Luo CB, Zhou ZJ, Xin HY, et al. A positive feedback loop between cancer stem-like cells and tumor-associated neutrophils controls hepatocellular carcinoma progression. *Hepatology* 2019;70:1214–30.
- Erpenbeck L, Schon MP. Neutrophil extracellular traps: protagonists of cancer progression? *Oncogene* 2017;36:2483–90.
- Brinkmann V, Reichard U, Goosmann C, Fauler B, Uhlemann Y, Weiss DS, et al. Neutrophil extracellular traps kill bacteria. *Science* 2004;303:1532–5.
- Garcia-Romo GS, Caielli S, Vega B, Connolly J, Allantaz F, Xu Z, et al. Netting neutrophils are major inducers of type I IFN production in pediatric systemic lupus erythematosus. *Sci Transl Med* 2011;3:73ra20.
- Raftery MJ, Lalwani P, Krautkrämer E, Peters T, Scharffetter-Kochanek K, Kruger R, et al.  $\beta$ 2 integrin mediates hantavirus-induced release of neutrophil extracellular traps. *J Exp Med* 2014;211:1485–97.
- Ren J, He J, Zhang H, Xia Y, Hu Z, Loughran P, et al. Platelet TLR4-ERK5 axis facilitates NET-mediated capturing of circulating tumor cells and distant metastasis after surgical stress. *Cancer Res* 2021;81:2373–85.
- Vorobjeva NV, Chernyak BV. NETosis: molecular mechanisms, role in physiology and pathology. *Biochemistry* 2020;85:1178–90.
- De Meo ML, Spicer JD. The role of neutrophil extracellular traps in cancer progression and metastasis. *Semin Immunol* 2021;57:101595.
- Papayannopoulos V. Neutrophil extracellular traps in immunity and disease. *Nat Rev Immunol* 2018;18:134–47.
- Yang L, Liu Q, Zhang X, Liu X, Zhou B, Chen J, et al. DNA of neutrophil extracellular traps promotes cancer metastasis via CCDC25. *Nature* 2020;583:133–8.
- Yazdani HO, Roy E, Comerci AJ, van der Windt DJ, Zhang H, Huang H, et al. Neutrophil extracellular traps drive mitochondrial homeostasis in tumors to augment growth. *Cancer Res* 2019;79:5626–39.
- Teijeira A, Garasa S, Gato M, Alfaro C, Migueliz I, Cirella A, et al. CXCR1 and CXCR2 chemokine receptor agonists produced by tumors induce neutrophil extracellular traps that interfere with immune cytotoxicity. *Immunity* 2020;52:856–71.
- Kaltenmeier C, Yazdani HO, Morder K, Geller DA, Simmons RL, Tohme S. Neutrophil extracellular traps promote T cell exhaustion in the tumor microenvironment. *Front Immunol* 2021;12:78522.
- Wang H, Zhang H, Wang Y, Brown ZJ, Xia Y, Huang Z, et al. Regulatory T-cell and neutrophil extracellular trap interaction contributes to carcinogenesis in non-alcoholic steatohepatitis. *J Hepatol* 2021;75:1271–83.
- Zhang Y, Chandra V, Riquelme Sanchez E, Dutta P, Quesada PR, Rakoski A, et al. Interleukin-17-induced neutrophil extracellular traps mediate resistance to checkpoint blockade in pancreatic cancer. *J Exp Med* 2020;217:e20190354.
- Eil R, Vodnala SK, Clever D, Klebanoff CA, Sukumar M, Pan JH, et al. Ionic immune suppression within the tumour microenvironment limits T cell effector function. *Nature* 2016;537:539–43.
- Roberts TL, Idris A, Dunn JA, Kelly GM, Burnton CM, Hodgson S, et al. HIN-200 proteins regulate caspase activation in response to foreign cytoplasmic DNA. *Science* 2009;323:1057–60.
- Chen CL, Wang Y, Huang CY, Zhou ZQ, Zhao JJ, Zhang XF, et al. IL-17 induces antitumor immunity by promoting beneficial neutrophil recruitment and activation in esophageal squamous cell carcinoma. *Oncoimmunology* 2017;7: e1373234.
- Park J, Wysocki RW, Amoozgar Z, Maiorino L, Fein MR, Jorns J, et al. Cancer cells induce metastasis-supporting neutrophil extracellular DNA traps. *Sci Transl Med* 2016;8:361ra138.
- Kessenbrock K, Krumbholz M, Schonermanck U, Back W, Gross WL, Werb Z, et al. Netting neutrophils in autoimmune small-vessel vasculitis. *Nat Med* 2009;15:623–5.
- Li P, Li M, Lindberg MR, Kennett MJ, Xiong N, Wang Y. PAD4 is essential for antibacterial innate immunity mediated by neutrophil extracellular traps. *J Exp Med* 2010;207:1853–62.
- Kolaczkowska E, Jenne CN, Surewaard BG, Thanabalasuriar A, Lee WY, Sanz MJ, et al. Molecular mechanisms of NET formation and degradation revealed by intravital imaging in the liver vasculature. *Nat Commun* 2015;6:6673.
- Thommen DS, Schumacher TN. T cell dysfunction in cancer. *Cancer Cell* 2018;33:547–62.
- Mousset A, Lecorgne E, Bourget I, Lopez P, Jenovai K, Cherfils-Vicini J, et al. Neutrophil extracellular traps formed during chemotherapy confer treatment resistance via TGF-beta activation. *Cancer Cell* 2023;41:757–75.
- Noubouossie DF, Whelihan MF, Yu YB, Sparkenbaugh E, Pawlinski R, Monroe DM, et al. In vitro activation of coagulation by human neutrophil DNA and histone proteins but not neutrophil extracellular traps. *Blood* 2017;129:1021–9.
- Kelley RK, Gane E, Assenat E, Siebler J, Galle PR, Merle P, et al. A phase 2 study of galunisertib (TGF- $\beta$ 1 receptor type I inhibitor) and sorafenib in patients with advanced hepatocellular carcinoma. *Clin Transl Gastroenterol* 2019;10:e00056.
- Liu K, Sun E, Lei M, Li L, Gao J, Nian X, et al. BCG-induced formation of neutrophil extracellular traps play an important role in bladder cancer treatment. *Clin Immunol* 2019;201:4–14.
- Sivanandham R, Brocca-Cofano E, Krampe N, Falwell E, Venkatraman SMK, Ribeiro RM, et al. Neutrophil extracellular trap production contributes to pathogenesis in SIV-infected nonhuman primates. *J Clin Invest* 2018;128:5178–83.
- Gu W, Zhang M, Gao F, Niu Y, Sun L, Xia H, et al. Berberine regulates PADI4-related macrophage function to prevent lung cancer. *Int Immunopharmacol* 2022;110:108965.
- Stadler SC, Vincent CT, Fedorov VD, Patsialou A, Cherrington BD, Wakshlag JJ, et al. Dysregulation of PAD4-mediated citrullination of nuclear GSK3 $\beta$  activates TGF- $\beta$  signaling and induces epithelial-to-mesenchymal transition in breast cancer cells. *Proc Natl Acad Sci U S A* 2013;110:11851–6.
- Tohme S, Yazdani HO, Al-Khafaji AB, Chidi AP, Loughran P, Mowen K, et al. Neutrophil extracellular traps promote the development and progression of liver metastases after surgical stress. *Cancer Res* 2016;76:1367–80.
- Derynick R, Turley SJ, Akhurst RJ. TGF $\beta$  biology in cancer progression and immunotherapy. *Nat Rev Clin Oncol* 2021;18:9–34.
- de Andrea CE, Ochoa MC, Villalba-Esparza M, Teijeira A, Schalper KA, Abengozar-Muela M, et al. Heterogenous presence of neutrophil extracellular traps in human solid tumours is partially dependent on IL-8. *J Pathol* 2021;255:190–201.